nature astronomy

Article

https://doi.org/10.1038/s41550-024-02294-9

Cygnus X-3 revealed as a Galactic ultraluminous X-ray source by IXPE

Received: 1 September 2023

Accepted: 10 May 2024

Published online: 21 June 2024

Check for updates

A list of authors and their affiliations appears at the end of the paper

The accretion of matter by compact objects can be inhibited by radiation pressure if the luminosity exceeds a critical value known as the Eddington limit. The discovery of ultraluminous X-ray sources has shown that accretion can proceed even when the apparent luminosity considerably exceeds this limit. A high apparent luminosity might be produced due to the geometric beaming of radiation by an outflow. The outflow half-opening angle, which determines the amplification due to beaming, has never been robustly constrained. Using the Imaging X-ray Polarimetry Explorer, we measured the X-ray polarization in the Galactic X-ray binary Cygnus X-3 (Cyg X-3). We found high, >20%, nearly energy-independent linear polarization orthogonal to the direction of the radio ejections. These properties unambiguously indicate the presence of a collimating outflow from the X-ray binary Cyg X-3 and constrain its half-opening angle to $\lesssim$15°. Thus, the source can be used as a laboratory for studying the supercritical accretion regime. This finding underscores the importance of X-ray polarimetry in advancing our understanding of accreting sources.

Cyg X-3 is one of the first sources discovered in the X-ray sky[1]. It is the brightest X-ray binary in radio wavelengths[2–4], with peak fluxes reaching 20 Jy, and one of the few X-ray binaries from which γ-ray emission has been detected[5,6]. Cyg X-3 is also exceptional from the point of view of population synthesis and evolutionary studies[7,8]. It is the only known Galactic source containing a compact object in a binary orbit with a Wolf–Rayet (WR) star. WR stars are evolved massive stars characterized by a hydrogen-depleted spectrum[9,10]. Cyg X-3 is also the progenitor of a double-degenerate system[8] that will become a source of gravitational wave emission in the distant future.

The optical counterpart is not visible because of the high absorption along the line of sight. The source is in the Galactic plane at a distance $D = 9.67^{+0.53}_{-0.48}$ kpc (refs. 11,12). The system parameters have been constrained based on radio, X-ray and infrared (IR) properties. Spatially resolved discrete radio ejections[13,14] are aligned in the north–south direction. Moreover, the position angle of the intrinsic IR polarization (which may be associated with scattering off the circumstellar disk[15] or with the jet[16]) agrees, within uncertainties, with the jet position angle. The orbital period $P_{\rm orb} = 4.79234$ h has been measured with high accuracy based on the prominent X-ray and IR flux modulations, as well as from the periodic Doppler shifts of the X-ray and IR lines[16–19], and is known to change rapidly over time[20,21]. Orbital variations are clearly pronounced in all wavelengths, from γ-rays to radio, and enable determination of the orbital inclination (Methods and Extended Data Figs. 1, 2 and 3). A recent comprehensive analysis of the orbital photometric variations in X-rays and IR[22] gave the most precise orbital inclination of the source, $i = 29.5° \pm 1.2°$. Estimates obtained using other methods, namely Doppler shifts of X-ray lines[18] and relativistic ejections[14,23], have consistently small inclinations.

Cyg X-3 swings between several X-ray spectral states, which are tightly linked to its radio properties (Extended Data Figs. 4 and 5)[24]. It spends most of the time in a hard X-ray, radio-quiescent state. In this state, the X-ray emission can be described by a power law with prominent fluorescent iron lines (Extended Data Fig. 6 and Methods). Occasionally, Cyg X-3 transitions to an ultrasoft spectral state, during which the spectrum is dominated by a black body and peaks at a few kilo-electronvolts. Transitions to this state are accompanied by major radio ejections, in which the highest observed radio fluxes are reached. The spectral transitions are thought to be related to changes in the accretion geometry. However, the exact geometrical configuration in each state and the physical reasons behind the changes are not known.

e-mail: alexandra.veledina@gmail.com

https://doi.org/10.1038/s41550-024-02294-9

Table 1 | Summary of contemporaneous X-ray and γ-ray observations

Facility	Energy (keV)	MJD−59,800	Average flux (keV cm^{-2} s^{-1})
IXPE	2–8	66–71, 83–89	0.96
		138–142	2.6
NICER	0.5–12	84–87	1.6
ART-XC	4–30	87	2.9
INTEGRAL	20–100	84–88	1.1
		138	0.9
NuSTAR	3–50	65–66	3.5
		138–139	6.0
AGILE	10^5 to 5×10^7	66–71, 83–89	<0.033
		138–142	<0.22
Fermi	10^5 to 10^8	62–73	$\lesssim$0.01

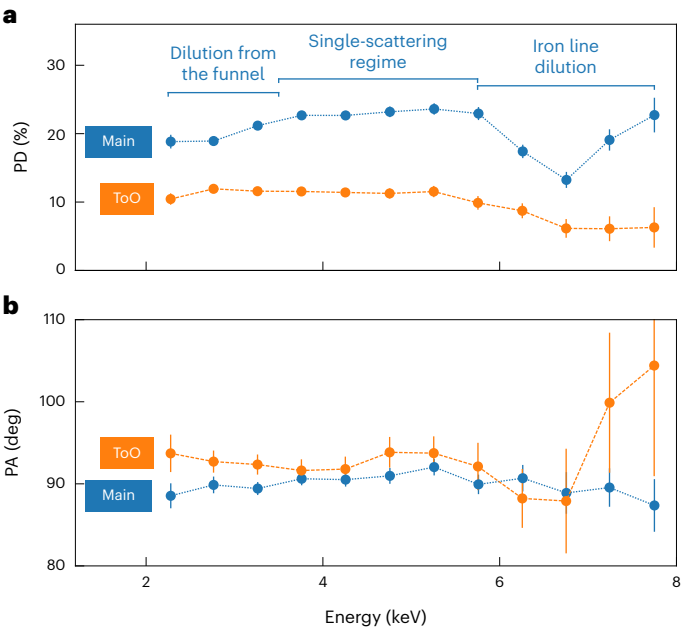

Fig. 1 | Orbital-phase averaged polarization properties from IXPE observations. a,b The energy dependences of the average PD (**a**) and average PA (**b**) are shown for the Main (blue lines) and ToO (orange lines) observations. In both cases, the PA is consistent with being constant across the energy range, and the PD is constant in the 3.5–6 keV band (null hypothesis probability values are 91% and 78% for the Main and ToO observations, respectively). The decrease of PD above 6 keV is caused by the contribution of the unpolarized iron line(s). PD is also lower below 3 keV for the Main observation, which may be related to the unpolarized contribution of reprocessed emission by the funnel walls (Methods). Data are given as the mean values in the selected energy band and the error bars correspond to 1σ confidence level.

Table 2 | Summary of radio and submillimetre observations

Telescope	Date MJD−59,800	Frequency (GHz)	Average flux (mJy)	Variance (mJy)	PD %	PA (deg)
SMA	71	225	76	36	2.8±1.1	−28±12
	85	225	86	35	2.2±0.4	−6±6
AMI-LA	63–90	15.5	106	27		
	137–139	15.5	126	24		
Medicina	66–70	8.4	118	26		
Effelsberg	61–70	8.3	99	16		
	61–70	6.3	99	12		
RATAN	84–88	8.2	142	15		
		4.7	106	24		
	138	4.7	107	36		
uGMRT	85–86	1.2	81	14		

IXPE observations were performed on MJDs 59,866–59,871, 59,883–59,889 and 59,938–59,942.

Understanding the physical picture of the system is complicated by the diversity of models that can explain the X-ray spectra. The quiescent-state spectra (corresponding to a hard X-ray continuum) can be fitted well with (1) an intrinsically soft spectrum severely absorbed in the WR wind, (2) a hard spectrum due to the hot medium within the truncated cold accretion disk (this model is often discussed in the context of other hard-state sources) or (3) equal contributions from the incident spectrum and the reflected emission[25,26]. Early works identified the potential importance of scattering of intrinsic emission in the formation of the observed spectra[27,28]. The models invoke very different emission mechanisms and a wide range of inherent luminosities and accretion rates, preventing us from identifying the accretion–ejection mechanisms of this unusual binary. The astronomical puzzle called Cyg X-3 (ref. 17) remained unsolved for over 50 years after its discovery, even though the system is one of the most frequently studied sources in the X-ray sky.

We report here on the detection of the X-ray polarization from Cyg X-3. Observations with the Imaging X-ray Polarimetry Explorer (IXPE)[29] revealed the accretion–ejection geometry of the source. The first IXPE observation (hereafter referred to as 'Main') caught the source in the hard X-ray (radio-quiescent) state and consisted of two runs, 14–19 October 2022 and 31 October to 6 November 2022 (Table 1). We found a high polarization degree PD = 20.6 ± 0.3% in the 2–8 keV range (Fig. 1). The polarization angle PA = 90.1° ± 0.4° (which is determined by the direction of electric field oscillations, measured from north through east on the sky) is orthogonal to the position angle of the discrete radio ejections and the IR and submillimetre polarization (Table 2)[13–15]. The observed PD is constant over the 3.5–6 keV range. The PD is lower in the 6–8 keV range, where the fluorescent and recombination Fe Kα emission lines dominate, as well as below 3 keV (Fig. 1a and Methods). The fluorescent lines originate from the transitions of the electrons to lower atomic levels of iron, and the distribution of the resulting photons and their electric vectors is expected to be isotropic, giving unpolarized emission.

We performed an orbital-phase-resolved analysis of the polarimetric data using the recent ephemeris (Methods). Note the large variations in the PA (Fig. 2) and a complex relation between the PA and PD variations (Methods and Extended Data Figs. 7 and 8). The pattern is not consistent with a model of scattering off optically thin plasma in an orbit with the X-ray source[30], for example, scattering off the wind close to the surface of the WR star. In this case, the low inclination of the system would lead to sinusoidal variations of the PA with two peaks per orbital period (equivalent to a double loop in the normalized Stokes parameters Q/I–U/I plane). Furthermore, the PD of the primary X-rays reflected off the star is expected to be <1%. For a distant reflector, the PD is small due to the small solid angle subtended by the star as seen from the compact object. For a higher solid angle of the scattering matter, namely if scattering proceeds within the WR wind, a low PD is also expected, as in this case the scatterers are nearly spherically symmetric.

The high, in excess of 20%, average PD and its orientation relative to the radio outflows suggest that the IXPE signal is dominated by

https://doi.org/10.1038/s41550-024-02294-9

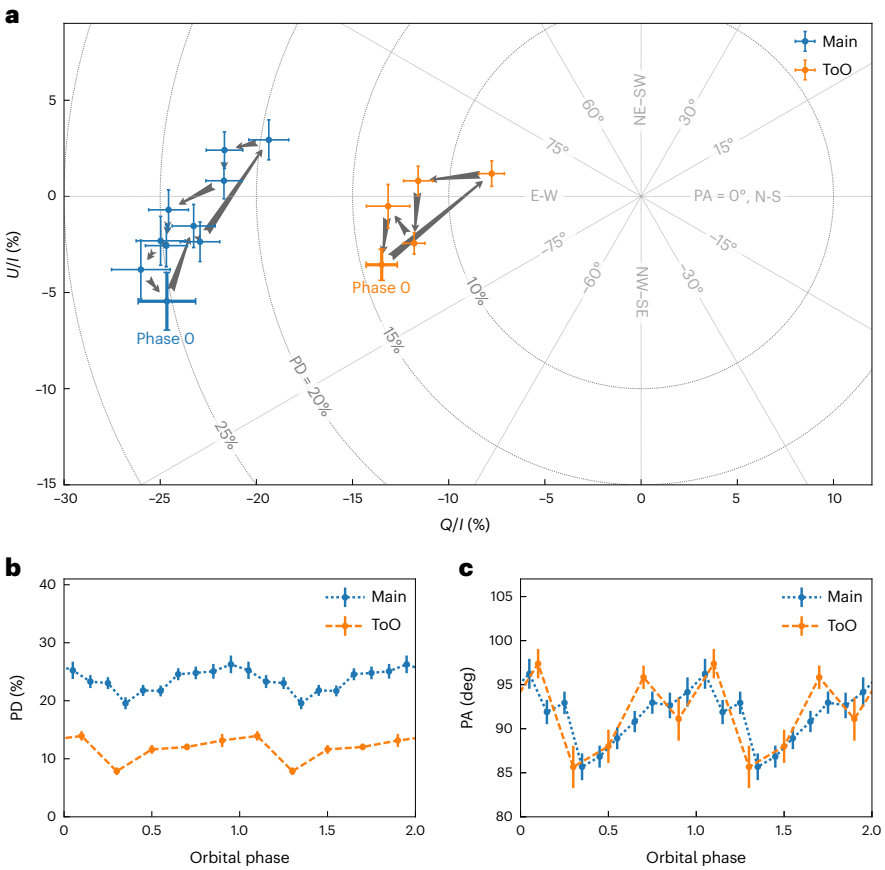

Fig. 2 | Orbital-phase-folded polarization properties. a, Evolution of the normalized Stokes parameters *U*/*I* versus *Q*/*I*. Blue corresponds to the Main observation and orange to the ToO observation. Arrows indicate the path followed by the data. Phase 0 corresponds to the superior conjunction. **b**,**c**, The dependence of the PD (**b**) and PA (**c**) on the orbital phase in the 3.5–6 keV energy range. Data are presented as mean values in the selected orbital-phase bin and the error bars correspond to 1σ confidence level.

the reflected component, with a minor to zero contribution from the primary continuum. Indeed, the Comptonization continuum cannot give such high polarization, and the synchrotron mechanism fails in explaining the multiwavelength polarization properties, namely that the PAs of submillimetre and IR polarization are orthogonal to the X-ray polarization. This conclusion is bolstered by our finding of a largely energy-independent polarization, as the superposition of comparable contributions from primary and reflected emission would lead to a strong energy dependence of the PD. Previous spectral modelling included scenarios with a substantial contribution from reflection to the total X-ray spectra[26]. However, the 2–8 keV spectra have never been considered to be completely dominated by reflection. To verify the possibility that the dominant contribution is from the reflection component in the IXPE band, we performed spectro-polarimetric modelling (Fig. 3). We used a model comprising a reflection continuum and a Gaussian component that mimics the contribution from an iron line complex at energies 6–7 keV. The PDs of both components and the PA of the continuum were free fitting parameters, whereas the PA of the Gaussian was fixed to the value found for the continuum (Methods). We found that the observed broadband spectral energy distribution could be approximated well (χ^2/ degrees of freedom (d.f.) = 936/881) by reflection of an intrinsically soft spectrum. The reflection continuum is highly polarized with constant PD = 22.8 ± 0.4%, and the line emission is unpolarized (with a 90% confidence level upper limit of 2%).

The polarization of Cyg X-3 closely resembles that of the accreting supermassive black hole in the Circinus galaxy, which exhibits PD = 28 ± 7% (ref. 31). For that source, the primary X-rays are believed

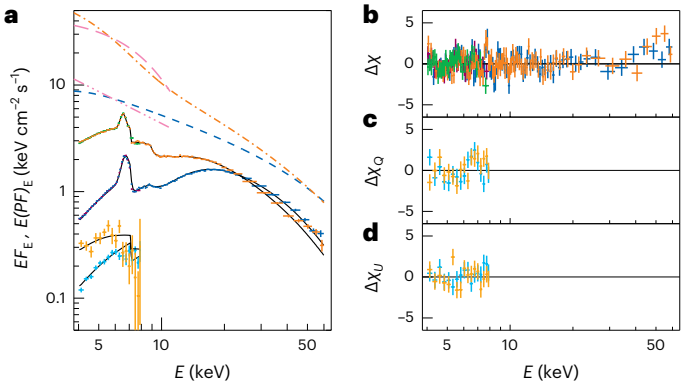

Fig. 3 | Average spectro-polarimetric data with the best-fitting models for the Main and ToO observations. a, The observed fluxes in EF_E units. NuSTAR Main (blue) and ToO (orange) and IXPE Main (violet) and ToO (green) observations. Note that the IXPE and NuSTAR points are nearly identical and, hence, may not be well distinguished in the plot. IXPE polarized fluxes $E(PF)_E = \mathrm{PD}(E)EF_E$ are shown for the Main (cyan) and ToO (yellow) observations. Black lines correspond to the fitting model for each dataset. Blue dashed and orange dot-dashed lines correspond to the intrinsic spectra that are needed to reproduce the observed reflected spectra for the Main and ToO datasets, respectively. Magenta long-dashed and triple-dot-dashed lines correspond to the illustrative intrinsic spectra of supersoft and soft ULXs (spectra and notations are adopted from ref. 35), overlaid on top of the intrinsic spectra of Cyg X-3 for comparison. **b**–**d**, Residuals of the data relative to the model, in units of the errors, for the flux (**b**), *Q* parameter (**c**) and *U* parameter (**d**). The error bars correspond to 1σ confidence level.

https://doi.org/10.1038/s41550-024-02294-9

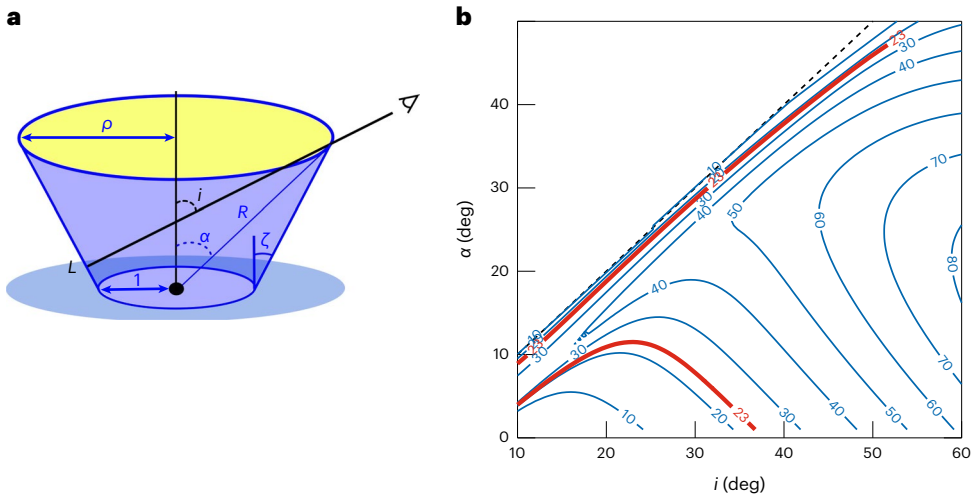

Fig. 4 | Geometry of the funnel and its polarization properties. a, Proposed geometry of the funnel with the primary emitting source marked by a filled black circle. The observer at inclination i sees the reflection from the inner surface of the funnel (down to point L). The primary source is obscured by the funnel walls. The half-opening angle of the funnel ζ is always smaller than the angle α, the latter being used as a proxy for ζ in the text. Radii are measured in units of the funnel base. **b**, Contour plot of constant PD for different observer inclinations i and parameter values α. Numbers in the lines denote polarization in per cent. The red contour marks the observed polarization of 23%.

to be obscured by a dusty torus with an inclination exceeding that of the host galaxy, $i \approx 65°$, so that the reflected emission dominates over the direct emission in the IXPE band. The obscuration of a system with a low orbital inclination $i \approx 30°$ (refs. 18,22,23) is not naturally expected. Our finding of a high, energy-independent PD leads to an important implication for the accretion geometry of Cyg X-3. As the observer does not see the primary X-ray source, we infer the presence of an optically thick medium high above the orbital plane, shaped like a funnel (Fig. 4). For the Thomson scattering (equation (1)), the observed PD translates to the typical scattering angle ~38°, which is close to the orbital inclination. Our modelling of the X-ray polarization indicates a narrow funnel with half-opening angle $\alpha \lesssim 15°$. Figure 4b shows contour plots of the PD as a function of α and i (see also Extended Data Figs. 9 and 10). We identified two branches of solutions (red lines). However, we excluded the upper branch based on the dependence of the orbit-averaged PD on time (Extended Data Fig. 1 and Methods).

Optically thick and elevated envelopes are hallmarks of super-Eddington accretion rates[32–34]. We checked this hypothesis by estimating the intrinsic X-ray luminosity of Cyg X-3 (Extended Data Fig. 9c). Assuming that the observed radiation comes from the visible inner part of the funnel, we can relate the reflected luminosity to the intrinsic one through the reflection albedo and the solid angle of the visible part of the funnel (alternatively, the scattering can proceed in the WR wind right above the funnel, but the resulting luminosities are the same; see more details in Methods). We found that the intrinsic luminosity exceeds the Eddington limit for a neutron star accretor at half-opening angles $\alpha \approx 8°$, whereas for $\alpha \approx 15°$, this limit is exceeded for a black hole of ten solar masses. Further, for the small opening angle of the funnel required by the polarimetric data, the apparent luminosity for an observer viewing down the funnel is $L \gtrsim 5.5 \times 10^{39}$ erg s^{-1} in the 2–8 keV range, which puts Cyg X-3 in the class of ultraluminous X-ray sources (ULXs)[35].

To identify the properties of the accretion geometry that drive the soft to hard state transitions in the source, we performed an additional IXPE target of opportunity (ToO) observation as the source transitioned towards the soft state, as indicated by the X-ray and radio fluxes, on 25–29 December 2022 (Methods). The ToO revealed a twice lower, largely energy-independent PD = 10.0 ± 0.5% at 2–8 keV, whereas PA = 90.6° ± 1.2° is like the value found in the Main observation (orange symbols in Figs. 1–3). In particular, this suggests that we continue to see the reflected signal in this state but that the funnel parameters have changed. In particular, the decreased polarization may suggest that the reflection and reprocessing now operate in some volume of matter around the funnel (within the outflow material), rather than coming solely from its surface. This is consistent with the outflow becoming more transparent, which may be related to the drop of the mass-accretion rate. We expect that a further decrease of the matter supply would lead to a collapse of the funnel. This would reveal the X-ray emission from the inner parts of the accretion disk and would be accompanied by a drop in its polarization. The spectrum in this case should closely resemble the one produced by the multicolour disk[32], which is indeed observed in Cyg X-3 during the so-called ultrasoft state. Our scenario suggests that this state corresponds to a lower accretion rate compared to the hard X-ray and radio-quiescent state, even though the source appears brighter. Following our findings, the whole complex of multiwavelength properties may need to be reconsidered in light of this renewed accretion geometry.

Narrow funnels have been used to explain the high apparent luminosity of ULXs[35–38]. However, determining the opening angles of the base of these ULX outflows has not been possible directly from observations, as the observer is close to the axis of the funnel and sees the strongly amplified radiation of the central source. Moreover, the Galactic supercritical counterparts are seen at high inclinations, such as $i \approx 78°$ for the persistent source SS 433 (ref. 39), $60° \lesssim i \lesssim 80°$ for the transient V404 Cyg, $i = 66° \pm 2°$ for GRS 1915+105 (refs. 40–42) and $i = 72° \pm 4°$ for V4161 Sgr (refs. 43,44), so that a thick outflow blocks the inner engine from our line of sight. The small inclination of Cyg X-3 system allows one to see the reflected and scattered components from the inner surface of the funnel, and the properties of X-ray polarization enable robust conclusions about the source geometry.

The X-ray polarimetric data probe the accretion geometry of Cyg X-3. These data have revealed that this famous and long-studied Galactic source has been accreting in the super-Eddington regime. This discovery opens a new chapter in the study of this exceptional system and establishes it as an analogue of distant ULXs and supercritical transients, such as tidal disruption events. We have directly constrained the half-opening angle of the outflow funnel of Cyg X-3 to be $\lesssim 15°$.

Methods

X-ray spectro-polarimetry analysis

The first attempt to detect the linear polarization of the X-rays from Cyg X-3 was made with the OSO-8 satellite[45], but the presence of other bright

sources in the field of view prevented the authors from reaching firm conclusions. IXPE[29] observed Cyg X-3 twice. The first and second observations are named 'Main' and 'ToO'. The Main observation was split into two observing periods close in time. The first started at 01:26:33 UTC on 14 October 2022 and ended at 14:12:56 UTC on 19 October 2022, and the second was carried out between 12:50:08 UTC on 31 October 2022 and 08:42:21 UTC on 6 November 2022. The ToO observation started at 10:05:17 UTC on 25 December 2022 and ended at 17:44:22 UTC on 29 December 2022. The durations of the Main and ToO observations were approximately 538 and 199 ks, respectively.

Our analysis of the IXPE data was carried out as for other observations (for example, see ref. 46). Level 2 (processed) data were downloaded from the IXPE archive managed by the High-Energy Astrophysics Science Archive Research Center (HEASARC). These data consist of three photon lists, one for each of the IXPE telescopes, and contain for each collected photon the time, position in the sky and the Stokes parameters of the single event. The arrival times of the photons were corrected to the Solar System barycentre using the barycorr tool from the ftools package, which is included in HEAsoft v.6.31, using the Jet Propulsion Laboratory's Development Ephemeris (DE421) and the International Celestial Reference System reference frame.

The source extraction region with a radius of 90 arcsec was centred on the source position. We did not attempt to extract the background from the remaining part of the field of view and subtract it from the source signal because the background in the IXPE field of view for relatively bright sources like Cyg X-3 is relatively weak and is dominated by contamination from source photons, which are focused in the outer wings of the mirror's half-power diameter[47]. Thus, removing the background in this case mostly removes a few per cent of the source signal.

Polarization can be obtained from the IXPE photon list with two approaches. The first builds the Stokes spectra $I(E)$, $Q(E)$ and $U(E)$, which are calculated by summing the relevant Stokes parameter for all the events in a specific energy bin. Such spectra can then be fitted with forward-fitting software by associating a polarization model with each spectral component[48]. For this, we used XSPEC v.12.13.0 (ref. 49). The second approach uses the IXPEOBSSIM package[50], which calculates the Stokes parameters as the sum of the event values in an energy, time or angular bin[51]. The latter approach does not assume any underlying spectral model. Data collected from the three IXPE telescopes were analysed separately by applying the appropriate response matrices (unweighted, version 12, in our case), which are available in the HEASARC calibration database (CALDB) and in the IXPEOBSSIM package.

The average polarization over the entire IXPE energy range (2–8 keV) was calculated with the PCUBE algorithm included in the IXPEOBSSIM/XPBIN tool. PD = 20.6 ± 0.3% and 10.4 ± 0.03% were found for the Main and ToO observations, respectively, with PA = 90.1° ± 0.4° and PA = 92.6° ± 0.7°, measured east of north.

A more detailed study of the X-ray polarization and its relation to various spectral components would require proper spectro-polarimetric modelling. The Nuclear Spectroscopic Telescope Array (NuSTAR) observatory provided broadband X-ray spectral coverage of Cyg X-3 during the Main and ToO runs. NuSTAR consists of two identical X-ray telescope modules, referred to as FPMA and FPMB[52]. It provides X-ray imaging, spectroscopy and timing in the energy range 3–79 keV with an angular resolution of 18 arcsec (full-width at half-maximum) and spectral resolution of 400 eV (full-width at half-maximum) at 10 keV. We used two NuSTAR datasets. The first was captured on 5 November 2022 (Observation ID 90802323004) with an on-source exposure of ~16 ks (during the Main observation). The second was captured on 25 December 2022 (Observation ID 90801336002) with ~36 ks exposure (during the ToO observation). Both observations covered several orbital cycles of the system, which allowed us to perform phase-resolved spectroscopy. The NuSTAR data were processed with the standard NuSTAR data analysis software (NuSTARDAS of 4 May 2021 v.2.1.1) provided in HEAsoft v6.29 with CALDB v.20201217. Circular 100 arcsec radius regions were used for both source and background spectra extraction. The source region was centred on the locations of Cyg X-3, and the background region was selected from a sourceless region in the detector image. All spectra obtained were grouped to have at least 25 counts per bin using the grppha tool. The final data analysis (timing and spectral) was performed with the software package HEAsoft v.6.29.

We performed broadband spectral modelling for both Main and ToO runs using the data from the NuSTAR and IXPE instruments. There is complexity in such modelling in light of the high-amplitude orbital variability. The small statistical errors in the spectra cause the average spectra to be unrepresentative, as the orbital variations of flux and hardness alter the average spectral shape. Furthermore, the lower energies contain prominent spectral lines, which are not well resolved in the IXPE band (Extended Data Fig. 6). Mutual contributions of the unpolarized lines may be responsible for the observed decrease of PD below 3 keV. Alternatively, the additional contribution of the incident X-ray radiation reprocessed by the funnel walls may be responsible for the visible decrease. For the aforementioned reasons, we added 1% systematic errors to the data and considered only data above 4 keV. For the Main observation, we found that a good fit can be obtained when summing all spectra (as the spectral shape does not evolve substantially with the orbital phase). For the ToO observation, we found that we could use only spectra averaged over orbital phases 0.25–0.75, that is close to the inferior conjunction, when the intrabinary absorption is smallest. As IXPE observed Cyg X-3 in a relatively bright state for a long time, the large number of events collected made evident the small systematic differences among the three IXPE telescopes, which mostly affected only the I spectrum. To account for these, we introduced a multiplicative power law (MPL) cross-calibration function, fE^{γ}, as was done for the analysis of the black hole Cyg X-1, also observed by IXPE[46]. For the Main observation, we left the gain and offset of the IXPE energy scale free to vary, whereas the offset for NuSTAR was as suggested by ref. 53.

Motivated by the polarization properties, we considered a model in which the spectrum is dominated by the reflection component. We used the XSPEC model reflect, which describes the reflection spectrum of the neutral matter[54] that is produced by the continuum. The latter is due to the multicolour accretion disk, as described by diskpbb (where the local black-body temperature has a power-law dependence on distance to the compact object and the power index is a free model parameter), and it includes a soft Comptonization continuum, as described by nthComp[55]. The shape of the continuum is like the soft spectra observed for ULXs[35,56,57]. We found that one Gaussian component can describe the line complex around 6.5 keV (see Extended Data Fig. 6 for more details). We fitted the data with the model constant × MPL × (polconst × reflect × smedge × (diskpbb + nthComp) + polconst × Gaussian). A similar model was previously used to fit the spectra of SS 433 (ref. 38) and the incident continuum was found to be similarly soft. We set the parameter rel_refl = −1, which means that we did not take the contribution of the incident X-ray emission into account in the resulting spectra. For the Main observation, the thermal component in the incident spectrum was not needed, so we set its normalization to zero. We realized an acceptable fit with χ^2/d.f. = 936/881 (Fig. 3 and Table 3).

The transition from the hard (radio-quiescent) to the intermediate (minor flaring) state in this model is related to the changing shape of the intrinsic continuum, which we nevertheless do not see directly but only from its reflection. To describe the spectra of the ToO observation, we need a softer incident X-ray spectrum, which is achieved by considering a non-zero contribution of the multicolour disk component. We realized an acceptable fit with χ^2/d.f. = 922/885. We found that the spectra can also be fitted with other models, including those in which the primary X-ray emission and reflection both substantially contribute to the X-ray continuum, thus repeating the diversity of models presented in ref. 26. We confirmed that the polarimetric information is vital when choosing from a variety of options. Finally, note that no

https://doi.org/10.1038/s41550-024-02294-9

Table 3 | Model parameters for the spectro-polarimetric fitting of the IXPE and NuSTAR data

Parameter	Main	ToO
polconst_refl A	$0.228^{+0.008}_{-0.005}$	$0.100^{+0.007}_{-0.008}$
polconst_refl psi (deg)	$90.9^{+0.6}_{-1.0}$	$90.6^{+2.5}_{-2.3}$
reflect rel_refl	−1.0 (frozen)	−1.0 (frozen)
reflect Redshift	0.0 (frozen)	0.0 (frozen)
reflect abund	1.0 (frozen)	1.0 (frozen)
reflect Fe_abund	$0.69^{+0.02}_{-0.04}$	$0.47^{+0.02}_{-0.06}$
reflect cosIncl	$0.23^{+0.11}_{-0.05}$	$0.051^{+0.013}_{-0.001}$
smedge edgeE (keV)	$8.66^{+0.08}_{-0.15}$	$8.83^{+0.08}_{-0.04}$
smedge MaxTau	$0.48^{+0.13}_{-0.03}$	$0.35^{+0.02}_{-0.06}$
smedge index	−2.7 (frozen)	−2.7 (frozen)
smedge width	$1.8^{+0.9}_{-0.3}$	$0.49^{+0.05}_{-0.11}$
diskpbb kT_{in} (keV)	–	$1.10^{+0.02}_{-0.03}$
diskpbb p	–	$0.50^{+0.05}_{-0.50}$
diskpbb norm (×10^3)	–	$7.9^{+0.9}_{-1.8}$
nthComp Gamma	$2.62^{+0.07}_{-0.03}$	$2.98^{+0.02}_{-0.06}$
nthComp kT_e (keV)	30^{+16}_{-5}	47^{+6}_{-11}
nthComp kT_{bb} (keV)	$0.62^{+0.03}_{-0.02}$	$1.21^{+0.05}_{-0.20}$
nthComp norm	$3.6^{+0.7}_{-0.8}$	$2.5^{+1.3}_{-0.3}$
polconst_gauss A	$0.00^{+0.02}$	$0.00^{+0.06}$
polconst_gauss psi (deg)	91 (linked)	91 (linked)
gaussian LineE (keV)	$6.64^{+0.01}_{-0.01}$	$6.53^{+0.02}_{-0.02}$
gaussian Sigma (keV)	$0.261^{+0.014}_{-0.013}$	$0.19^{+0.03}_{-0.02}$
gaussian norm (×10^{-3})	$12.76^{+0.44}_{-0.37}$	$17.1^{+1.7}_{-1.1}$
IXPE/det1_constant factor	$1.76^{+0.11}_{-0.06}$	
IXPE/det2_constant factor	$1.62^{+0.10}_{-0.06}$	
IXPE/det3_constant factor	$1.63^{+0.10}_{-0.06}$	
IXPE_mpl gamma	$0.29^{+0.04}_{-0.02}$	
IXPE/det1 gain slope	$0.9990^{+0.0012}_{-0.0005}$	–
IXPE/det1 gain offset (keV)	$-0.054^{+0.006}_{-0.004}$	–
IXPE/det2 gain slope	$0.9790^{+0.0004}_{-0.0012}$	–
IXPE/det2 gain offset (keV)	$0.083^{+0.004}_{-0.007}$	–
IXPE/det3 gain slope	$0.9948^{+0.0006}_{-0.0013}$	–
IXPE/det3 gain offset (keV)	$-0.031^{+0.004}_{-0.007}$	–
NuSTAR gain slope	1.0 (frozen)	–
NuSTAR gain offset (keV)	$-0.103^{+0.007}_{-0.001}$	–
χ^2/d.f.	935.77/881	921.63/885

The model is constant×MPL×(polconst×reflect×smedge×nthComp+polconst×Gaussian). Uncertainties were calculated with the XSPEC/ERROR command at 90% confidence level.

currently available public model can account for the complex properties of the reflection in the proposed scenario. As we used a complex incident spectrum, we need to use a convolution model that considers a hydrogen-poor material and can self-consistently account for the lines.

The spectro-polarimetric modelling results for the Main and ToO observations are shown in Fig. 3. The model parameters are reported in Table 3. As we are interested in the overall shape of the intrinsic spectra, note that these parameters are to be considered as guiding, as the set of values may not be unique. Figure 3a also has plots of the illustrative spectra of (the so-called supersoft and soft) ULXs[35], which match well the shape of intrinsic spectra of Cyg X-3. The normalization of the intrinsic spectra and ULX spectra are free parameters. For both the Main and ToO observations, the polarization of the prominent line associated with the complex of iron lines is consistent with zero to account for the reduction of the measured PD at those energies. We also found that a line polarization of 9.4 ± 3.0% oriented orthogonal to the continuum polarization provides an acceptable spectro-polarimetric fit, with χ^2 = 928.13 for 880 d.f. Like an unpolarized line, this could account for the reduction of the observed polarization in the high-energy part of the IXPE energy range. Albeit the improvement is statistically significant (the F statistic is 7.2 for a chance probability of 0.7%), we consider this fit to be affected by the systematic uncertainties of our analysis. This scenario is also difficult to understand from the physical point of view, and therefore, we will not discuss it further. The primary continuum (reflection component) is highly polarized, 22.8 ± 0.4% for the Main observation and 10.0 ± 0.5% for the ToO.

It is well known that Cyg X-3 exhibits a large modulation in flux with the orbital phase of the binary system[20,22]. To investigate possible variations in polarization, we folded the IXPE observations of the source with the ephemeris in Table 2 (second model) of ref. 21. Phase 0 identifies the superior conjunction of the system, in which the compact object is behind the WR star. The data were grouped into ten (five) phase bins for the Main (ToO) observation, and the polarization was calculated with the IXPEOBSSIM/XPBIN algorithm in three energy bands, 2–3.5, 3.5–6 and 6–8 keV. These were chosen to highlight, in the energy range of IXPE, the contributions of the main spectral features identified in the spectro-polarimetric modelling. The phase-folded PD and PA are shown in Extended Data Fig. 7. Both have evident orbital variations, which are consistent among the three energy ranges. The PA variations are nearly sinusoidal with an amplitude of approximately ±5°, for both the Main and ToO observations, whereas the PD variations are more irregular with an amplitude of a few per cent. The average PD measured by the ToO was a factor of two lower with respect to the Main observation and shows similar but not identical orbital profiles.

Note that, excluding variations due to the orbital phase, the polarization remains stable over time. This is shown in Extended Data Fig. 1, which compares the measured PD and PA over the total IXPE energy range with time bins of one period, together with flux variations during the IXPE Main observation. Although the latter varied significantly, the PD and PA varied around their average values within the statistical uncertainties. This suggests that the geometry that defines the high polarization observed for Cyg X-3 is stable with time and essentially unrelated to the ultimate mechanisms producing the X-ray variability on superorbital timescales.

Multiwavelength data

Cyg X-3 has been observed frequently over the past decades from radio through γ-rays. Over long timescales of weeks to months, the source evolves through the sequence of distinct X-ray and radio spectral states (Extended Data Fig. 4 and refs. 24,58). The most frequent state is the hard X-ray, radio-quiescent state, which corresponds to the lowest observed X-ray flux. We observed the source in this state during the Main IXPE run (Extended Data Fig. 5). The absorption within the binary is uncertain. Hence, different branches of spectral models, corresponding to different geometries and dominant spectral components, have been proposed[25,26], including models in which the incident power-law-like Comptonization spectrum is heavily absorbed or downscattered in the stellar wind, models with nonthermal Comptonization produced by a steep electron distribution and models dominated by

the reflection component with a geometry such that the reflector partially covers the primary X-ray source. This diversity of alternatives has prevented previous efforts from reaching firm conclusions on the intrinsic luminosity in this state, which is always found to be of the order of 10^{38} erg s^{-1}, but the precise numbers vary by a factor of 4–5, depending on the model. Moreover, the uncertainty regarding the mass of the compact object[18,22,59–61], along with its nature (a neutron star or a black hole), and the chemical composition of the hydrogen-poor matter dragged from the WR companion likewise lead to various estimates of the Eddington luminosity. It is, therefore, unclear as to what kind of accretion regime to expect in this state.

The source occasionally displays spectral transitions to the soft state, which is followed by an increase of the soft X-ray luminosity and suppression of the radio emission (to levels below those observed in the radio-quiescent state). The changes to the spectral shape have been attributed to changes of the accretion–ejection geometry. The X-ray spectra of the soft and ultrasoft states resemble thermal emission from a multicolour accretion disk[32], which is typically seen at luminosities between the Eddington limit and down to 10% of it. After the transition, a major radio flare may happen, and it reaches the highest radio fluxes of all X-ray binaries[4,62]. The second IXPE run was triggered as a target of opportunity observation following the increase of the soft X-ray flux and the drop in the radio fluxes, which occurred when the source transited to the suppressed radio state. IXPE caught the source after the radio flux had recovered. It was in its intermediate X-ray state, during the minor flaring radio episodes (Extended Data Fig. 4)[24].

On shorter timescales, a prominent orbital variability of the X-ray, γ-ray, IR and radio fluxes[22,63–66] and the X-ray and IR line shapes[16,18,19,67] has been observed. Our multiwavelength observations show orbital flux variations in all bands (Extended Data Figs. 2 and 3). The lack of apparent variations in the absorbing column density over the orbital phase (noted in ref. 19) suggests that the mean orbital modulation is not primarily caused by the line-of-sight absorption variations of the low-density and partly ionized gas, such as WR wind. Either scattering in an ionized gas or the asymmetric geometry of a reflector[19,28] may be more important. Moreover, the hard-state modulation amplitude depends on the X-ray energy[68], suggesting that scattering alone may not be responsible for the variations. The X-ray orbital profiles are asymmetric[22,69], and the phase of the minimal X-ray flux does not necessarily coincide with the superior conjunction (with the compact object behind the WR star). A recent study suggests that these phases are close, with $\phi_{sc} = -0.066 \pm 0.006$ (ref. 22). Extended Data Fig. 6 shows the evolution of the lower-energy spectra observed with the Neutron Star Interior Composition Explorer (NICER) throughout the orbital phases during the October to November multiwavelength campaign. In broad agreement with previous results[19], we found that changes in the spectra as functions of the orbital phase did not follow a simple pattern of changing absorption, as in this case the spectral shape was expected to change substantially. Instead, we mostly saw variations of the spectral normalization, which are more in line with changes in the characteristic reflection angle[70].

At all phases, the energies 6–8 keV were dominated by the complex of the iron emission lines (Fe K lines). This complex consists of neutral iron, iron XXV and XXVI (refs. 18,19,61). The behaviour of these lines with the orbital phase varies and allows one to relate the hydrogen-like iron with the compact object[18]. An analysis of the ratios of the forbidden, resonance and intercombination lines indicates that they are produced in a dense medium, which nevertheless has high ionization[19]. Interestingly, the Chandra/HETGS spectrum of Cyg X-3 is so far the only fully resolved Fe K complex in an astrophysical source[61].

Supporting X-ray and γ-ray observations. NICER made contemporaneous observations of Cyg X-3 during the Main run. NICER is a soft X-ray instrument onboard the International Space Station, which was launched in June 2017. It consists of 56 co-aligned concentrator X-ray optics, each of which is paired with a single silicon drift detector. It is non-imaging but has a large collecting area and provides unmatched time resolution in the soft X-ray band-pass. Moreover, it is sensitive across 0.2–12 keV. NICER provided monitoring during the IXPE campaign, observing Cyg X-3 between MJDs 59,884 and 59,887. The resulting average and orbital-phase-resolved spectra are shown in Extended Data Figs. 5 and 6. Fluxes were obtained from best fits to these time-sequential data using an analogous model to that from the spectro-polarimetric fits in Table 3. NICER has good capabilities for timing studies. We checked for short-term variability (of the order of seconds) but did not find any significant intrinsic fluctuations above the noise level. This is in line with previous findings[71].

The Mikhail Pavlinsky ART-XC telescope carried out one observation of Cyg X-3 on 4 November 2022 (MJD 59,887) simultaneously with IXPE, with an 86 ks net exposure. ART-XC is a grazing incidence focusing X-ray telescope onboard the Spectrum-Rontgen-Gamma (SRG) observatory[72]. The telescope includes seven independent modules and provides imaging, timing and spectroscopy in the 4–30 keV energy range with a total effective area of ~450 cm^2 at 6 keV, angular resolution of 45 arcsec, energy resolutions of 1.4 at 6 keV, and timing resolution of 23 μs (ref. 73). ART-XC data were processed with the analysis software ARTPRODUCTS v1.0 and CALDB v.20220908. The ART-XC observation was performed approximately one day before the first NuSTAR observation (Main). Therefore, the spectral parameters measured by ART-XC are close to those determined from NuSTAR data, with a flux of ~4.6×10^{-9} erg cm^{-2} s^{-1} in the 4–30 keV energy band.

INTEGRAL observed Cyg X-3 simultaneously with IXPE twice. The first observation lasted from 21:11 UT on 1 November 2022 to 20:23 UT on 5 November 2022. The second observation lasted from 02:37 to 14:53 UT on 25 December 2022. Our data analysis was focused on ISGRI, the low-energy part of the IBIS telescope[74,75]. The INTEGRAL data were reduced using the latest release of the standard On-line Scientific Analysis package (v.11.2), which is distributed by the INTEGRAL Science Data Centre[76] through the Multi-Messenger Online Data Analysis platform[77]. The ISGRI spectra were extracted in the range 30–150 keV with a response matrix with 16 standard channels. The spectra of the first and the second observations were fitted with a simple power law with photon indices of 3.6 ± 0.1 (χ^2/d.f. = 18.3/21) and 3.4 ± 0.1 (χ^2/d.f. = 22.4/21), respectively. The fluxes in the range 20–100 keV were 1.7×10^{-9} and 1.4×10^{-9} erg cm^{-2} s^{-1}, respectively.

The Fermi/LAT data on Cyg X-3 were collected from 10 to 21 October 2022 (MJDs 59,862–59,873) in the 0.1–500 GeV energy band. Fermi is in a low Earth orbit with a 90 min period. It normally operates in survey mode, which allows the instrument to cover the whole sky in approximately 3 h (see full details of the instrumentation in ref. 5). A standard binned likelihood analysis[78] was performed with the latest available Fermitools v.2.0.8 software. The analysis was carried out using the latest Pass 8 reprocessed data (P8R3)[79] for the SOURCE event class (maximum zenith angle 90°) taken at the region centred at Cyg X-3 coordinates. The analysis was based on fitting a spatial and spectral model over a 14° radius region around the source. The model of the region included all sources from the 4FGL DR3 catalogue[80], as well as components for isotropic and Galactic diffuse emissions given by the standard spatial and spectral templates iso_P8R3_SOURCE_V3_v1.txt and gll_iem_v07.fits.

The spectral template for each 4FGL source present in the model was selected according to the catalogue. The normalization of the spectra of all sources, as well as the normalization of the Galactic diffuse and isotropic backgrounds, was assumed to be free parameters. Also note that Cyg X-3 is present in the 4FGL catalogue as 4FGL J2032.6+4053, a point-like source with a log-parabola-type spectrum. Following the recommendation of the Fermi-LAT Collaboration, we performed the analysis with energy dispersion handling enabled. To minimize potential effects from sources beyond the considered region of interest, we also included in the model all the 4FGL sources up to 10° beyond

this radius, with all the spectral parameters fixed to their catalogue values. The results of the described analysis, which used relatively narrow energy bins, are shown in Extended Data Fig. 5. The source was not detected in any of the selected energy bins at higher than 2σ significance (test statistic 4.0). The upper limits shown correspond to a 95% false-chance probability and were calculated with the IntegralUpperLimit Python module provided within Fermitools.

Cyg X-3 was also observed in γ-rays with Astrorivelatore Gamma ad Immagini Leggero (AGILE). The AGILE satellite[81] is a space mission of the Italian Space Agency (ASI) devoted to X-ray and γ-ray astrophysics. It has been operating since 2007 in a low Earth equatorial orbit. In its spinning observation mode, AGILE monitors about 80% of the entire sky with its imaging detectors every 7 min. The data collected with the γ-ray imager (GRID, 30 MeV to 50 GeV) were analysed over the periods for MJDs 59,866–59,871, 59,883–59,889 (Main) and 59,938–59,942. The data analysis was carried out using the latest available AGILE-GRID software package (Build 25), the FM3.119 calibrated filter, H0025 response matrices and the consolidated archive (ASDCSTDk) from the AGILE Data Center at the Space Science Data Center[82]. We applied South Atlantic Anomaly event cuts and 80° Earth albedo filtering by taking into account only incoming γ-ray events with an off-axis angle lower than 60°. The flux was calculated using the AGILE multi-source likelihood analysis software[83] based on the test statistic method[78]. We performed the multi-source likelihood analysis for Cyg X-3 by including, as background sources, the three nearby pulsars of the Cygnus region (PSR J2021+3651, PSR J2021+4026 and PSR J2032+4127), which are known to be persistent and intense γ-ray emitters. These are at angular distances of less than 5° from the source. For the background sources, we assumed the long-term integration spectra, as reported in the 2AGL catalogue[84]. We modelled the γ-ray spectrum for Cyg X-3 with a simple power law with a standard 2.0 photon index. The source was in the quiescent and intermediate state during the time of IXPE observations. Hence, no prominent γ-ray activity was detected. The full-band AGILE-GRID upper limits are given in Table 1 and are consistent with the Fermi/LAT limits. Spectral upper limits (50 MeV to 3 GeV) are shown in Extended Data Fig. 5.

Supporting radio and submillimetre observations. Monitoring of Cyg X-3 at radio wavelengths contemporaneous with IXPE was performed using the Large Array of the Arcminute MicroKelvin Imager (AMI-LA), RATAN-600, Medicina, Effelsberg, upgraded Giant Metrewave Radio Telescope (uGMRT) and Submillimeter Array (SMA) telescopes. This coverage allowed us to identify the state of the source, produce the broadband spectrum and place constraints on the PA at longer wavelengths. A summary of these observations can be found in Table 2 and in Extended Data Fig. 3.

Cyg X-3 was observed at 15.5 GHz with AMI-LA[85,86] during the IXPE observing campaigns. AMI-LA consists of eight 13-m antennas, which measure one polarization (Stokes $I + Q$) over a wide bandwidth of 12–18 GHz in eight broad channels. The observations were usually ~1 h long, with some longer observations, up to ~6 h, from 3 to 6 November. Each observation consisted of 10-min scans of Cyg X-3, interleaved with short observations of a nearby compact calibrator source J2052 + 3635, which was used to apply phase corrections and monitor the sensitivity of the telescope. The data were processed using standard procedures: (1) bad data due to various technical problems and interference were automatically eliminated, (2) any remaining interference (including the end channels, which were more prone to interference) and periods of heavy rain were manually edited, (3) the interleaved observations of J2052 + 3635 were used to provide the initial phase calibration of each antenna in the array throughout each observation and (4) the overall flux density scale was set by comparison with daily observations of the standard calibrator source 3C 286, together with the 'rain gauge' measurements made during the observations to correct for the varying atmospheric conditions[85]. Flux densities at 15.5 GHz were derived for 10-min averages from the central six broad frequency channels (covering 13.6–17.4 GHz). The resulting light curves are shown in Extended Data Fig. 3a,d.

To monitor Cyg X-3, we triggered a target of opportunity programme with the 32-m Medicina radio telescope so that we could follow the evolution of the radio emission during the IXPE observations. We carried out observations at the central frequency of 8.4 GHz (X band) with the total power continuum back end on 14–18 October 2022. Each session lasted 5 h per day and tracked the fast flux density variations, even during the quiescent state. We performed on-the-fly cross-scans and mapping along the right ascension and declination directions, setting a bandwidth of 230 MHz to avoid the strongest radio-frequency interference. Scans were performed along a length of 0.7° at a velocity of 2.4° min^{-1} at 8.4 GHz, with a sampling time of 40 ms. Data were calibrated through repeated cross-scans centred on NGC 7027 at different elevations. This calibrator has the advantage of being very close in elevation to the target. We extrapolated the calibrator flux density according to ref. 87. The calibration procedure included corrections for the frequency-dependent gain curves and compensation for the pointing offset measured on each scan. The data analysis was performed with the Single-Dish-Imager software, which was designed to perform automated baseline subtraction, radio-interference rejection and calibration[88]. We estimated the final accuracy of our measurements to be ~8% at 8.4 GHz. The resulting light curve is presented in Extended Data Fig. 3b.

Cyg X-3 was also observed with the 100-m Effelsberg dish on 9, 13, 14 and 18 October 2022 with the S45mm-receiver and the spectro-polarimeter back end. Acquisitions were performed over two bands, 5.4–7.2 (f_{centre} = 6.3 GHz), and in two sub-bands of the second band 7.6–8.2 and 8.4–9.0 GHz (f_{centre} = 8.3 GHz). These frequency ranges (especially the omission of the centre part of the second band) were chosen to avoid radio-frequency interference. We measured the flux density with the cross-scans method, doing several subscans in azimuth and elevation (12 for Cyg X-3). All subscans were corrected for pointing offsets and averaged. After that, the atmospheric absorption and the loss of sensitivity due to gravitational deformation of the dish were corrected (both effects were rather small). The final calibration was done with suitable flux density calibrators (3C 286 and NGC 7027). For the polarization, instrumental effects were corrected by a Müller matrix method. A number of calibrators were observed before and after the actual observations of Cyg X-3 to determine the various effects properly. No polarization was detected in the Effelsberg data, so that the level of polarization must have been lower than 5%. The resulting light curves are shown in Extended Data Fig. 3b,c.

Cyg X-3 was monitored daily at 4.7 and 8.2 GHz (ref. 89) by the north sector of the RATAN-600 telescope using the uncooled tuned receiver in the total power radiometer mode[90]. This mode allows one to perform sensitive observations, with precision being limited by radio-frequency interference. A typical accuracy of 5% for fluxes near 100 mJy was reached during the contemporaneous observations with IXPE. The main parameters of the antenna (effective area and beam size) were calibrated with the source NGC 7027. Observations of NGC 7027 in multi-azimuthal mode gave a flux density of 5.38 Jy at 4.7 GHz, in agreement with the standards[87]. Additional intraday observations of Cyg X-3 at 4.7 and 8.2 GHz were carried out with the southern sector and flat mirror configuration. The increased field of view (±30° compared to the observations with the north sector) in this configuration allowed one to follow the source longer. For discrete antenna configurations (with steps of 2°), we carried out 31 measurements, taken every 10 min. The resulting light curves at 4.7 and 8.2 GHz are shown in Extended Data Fig. 3b,c for the Main run and in Extended Data Fig. 3e for the ToO run.

Observations of Cyg X-3 during the Main IXPE observation with uGMRT were performed during the director discretionary time requested. Due to scheduling constraints, the observations were granted only for 2 and 3 November for ~5 h each, that is a full orbit.

Observations were performed in band 5 (1–1.4 GHz) using a correlation bandwidth of 400 MHz and 2,048 frequency channels. The observing strategy featured cross-scans on the source interleaved with calibrators for phasing and flux references. The absolute flux density scale was tied to the Perley–Butler 2017 scale. The CAPTURE pipeline[91] was used to analyse the GMRT data. The error on the total flux density of the source includes the error on the Gaussian fit and an absolute flux density error of 10% added in quadrature.

Cygnus X-3 was observed by the SMA on Maunakea in Hawaii on 19 October 2022 and 2 November 2022. The SMA observations used two orthogonally polarized receivers, which were tuned to the same frequency range in the full polarization mode. These receivers are inherently linearly polarized but are converted to circular using the quarter-wave plates of the SMA polarimeter[92]. The lower and upper sidebands covered 209–221 and 229–241 GHz, respectively. Each sideband was divided into six chunks with a bandwidth of 2 GHz and a fixed channel width of 140 kHz. The SMA data were calibrated with the MIR software package. Instrumental polarization was calibrated independently for the lower and upper sidebands and removed from the data. The polarized intensity, PA and PD were derived from the Stokes *I*, *Q* and *U* parameters. MWC 349 A and BL Lac were used for both flux and polarization calibration and Neptune was used for flux calibration. The observations on 19 October were done with four antennas and a median 225 GHz opacity of ~0.2, whereas those on 2 November were obtained with seven antennas and a median opacity of ~0.1. Due to the low level of polarization, the overall polarization measurements have low statistical significance, especially the 19 October observation. For that observation, it was necessary to exclude one of the four antennas. For the 2 November observation, data after 9.2 UT were excluded due to a substantial increase in the phase instability as a result of weather conditions. The overall flux uncertainty in an absolute sense is ~5% of the continuum flux value. The values shown in Table 2 are averages over the entire observation of that day. Light curves of the total intensity (Stokes *I*) for the 2 days are shown in Extended Data Fig. 3a.

Modelling

Analytical modelling of the funnel. At high accretion rates, the accretion disk possesses a critical point, the spherization radius, at which matter can leave the disk pushed by radiation pressure forces[32,33]. This forms an axially symmetric outflow with an empty funnel around the disk axis. Radiation emitted by the accretion disk cannot escape freely but is collimated by the funnel walls. As a result, an observer looking along the funnel will see strongly amplified emission[36]. On the other hand, an observer at a large inclination angle to the axis will see the photosphere that is located at a considerable distance from the central source. This depends on the mass-loss rate, which, in turn, depends on the accretion rate[33]. Such an observer can see radiation scattered and reflected from the funnel walls at high elevations where the matter is mostly neutral (the flux from the central source is expected to be reduced due to the small solid angles of matter on the plane of the sky and because of the collimation of the incident emission at the bottom of the funnel).

We approximated the funnel geometry with a truncated cone (Fig. 4a and Extended Data Fig. 9a), which has two main parameters: R, the distance to the X-ray photosphere at which the optical depth becomes comparable to unity, which is scaled to the inner radius of the outflow in the accretion disk plane, and the angle α at which the upper boundary of the funnel is seen from the primary X-ray source. Unpolarized radiation emitted by the central source (which is the inner accretion disk and the collimated radiation from the inner part of the funnel) impinges on the wall higher up in the funnel. The probability of photons being reflected is proportional to the energy-dependent single-scattering albedo λ_E, which is the ratio of the scattering opacity to the total (scattering and photo-electric) opacity. Because in the IXPE range $\lambda_E \ll 1$, the reflected radiation is dominated by single-scattered photons (multiple-scattering orders contribute to the observed spectrum if $\lambda_E \approx 1$). This radiation is polarized, with the PD for Thomson scattering (valid in the IXPE range) being dependent on the cosine of the scattering angle μ as

$$P(\mu) = \frac{1-\mu^2}{1+\mu^2}. \quad (1)$$

The PA of this radiation, which we denote as χ_0, is perpendicular to the scattering plane. The intensity of reflected radiation is proportional to the phase function $\frac{3}{4}(1+\mu^2)$ and the ratio $\eta_0/(\eta+\eta_0)$ (page 146 in ref. 93), where η_0 is the cosine of the angle between the local normal to the funnel wall and the incoming radiation beam and η is the cosine of the angle between the direction to the observer and the normal. Thus, the Stokes parameters representing the linearly polarized reflected radiation are

$$\begin{pmatrix} I_E \\ Q_E \\ U_E \end{pmatrix} = \lambda_E \frac{3}{4}(1+\mu^2)\frac{L_E}{4\pi r^2}\begin{pmatrix} 1 \\ P\cos 2\chi_0 \\ P\sin 2\chi_0 \end{pmatrix}\frac{\eta_0}{\eta+\eta_0}, \quad (2)$$

where L_E is the luminosity of the central object and r is the distance from the centre to the element of the funnel. Integrating this expression over the visible surface of the funnel, we get the observed flux and the corresponding Stokes parameters. We see that all Stokes parameters in the single-scattering approximation are proportional to λ_E and, therefore, the PD of the total radiation not dependent on the energy.

A natural condition for the primary source to be obscured is $i > \alpha$. Figure 4b shows contours of constant PD as functions of α and i, for a chosen $R = 10$. Two branches of solutions are possible for $i \lesssim 40°$: the lower branch with a narrow funnel $\alpha \approx 10°$ and an upper branch with $\alpha \approx i$, where the observer looks almost along the funnel walls. Note the tightly packed contours near this branch. These indicate that any small variation of the opening angle, such as a few degrees, would cause changes in the observed PD by tens of per cent. In contrast, the time dependence of the observed PD, averaged over the orbital phase, is consistent with being constant, with a standard deviation of 2.5% (Extended Data Fig. 1).

Extended Data Fig. 9b shows the dependence of PD parameters α and R, for $i = 30°$ (for other possible values of i, the topology and resulting numbers are similar). We see the same two branches of a possible solution corresponding to PD = 23% and consider only the lower one for the aforementioned reason (small observed variations of PD). The part of the diagram below $R = 1/\sin\alpha$ is forbidden, because it corresponds to $\rho < 1$, that is a converging towards the axis outflow. For the observed PD, the minimum possible size of the photosphere is $R = 8$, which corresponds to $\alpha = 8°$. At a larger R, the required α increases, saturating at ~15°.

The computed PDs in Fig. 4b and Extended Data Fig. 9b correspond to when polarization is produced solely at the inner surface of the funnel, which can be realized for a very high Thomson optical depth. These conditions may be applicable to the Main observation. The changes in the polarization properties during the ToO observation may have been caused by the reduction of the Thomson optical depth of the funnel. In this case, we would expect to see scattered radiation from some volume around the funnel walls, rather than solely from its inner surface. This would increase the role of photons scattered at small angles, and hence, it would lead to a reduction of the net polarization. Alternatively, the scattering may proceed right above the funnel, in the optically thin WR wind. Our estimates of the Thomson optical depth from the mass-loss rate and wind velocity, assuming hydrogen-poor material[22], give $\tau_{T,WR} \approx 0.1$–0.5. For a small optical depth, $\tau_{T,WR} \approx 0.1$, the spectrum of the scattered radiation would closely resemble that of the incident continuum. However, the observed spectral shapes do not

correspond to the spectra of any other unobscured accreting source. For larger $\tau_{T,WR} \approx 1$, on the other hand, the effect of multiple scattering tends to decrease the PD towards higher energies within the IXPE range, which is not consistent with the results of our spectro-polarimetric modelling. Thus, to be consistent with the data, this scenario requires tight constraints, $\tau_{T,WR} \approx 0.3–0.5$, which might be hard to realize. Our calculations show that the resulting PD in this scenario is nearly independent of the funnel angle α at any inclination $i > \alpha$. Hence, this case cannot account for the change in the PD between the Main and ToO observations, as changes of the $\tau_{T,WR}$ within the allowed narrow range would lead to variations of only the flux and not the PD. If we consider this scenario for the ToO observation, then the observed PD ≈ 10% translates to an inclination $i \approx 25°$ according to equation (1).

An important property of the observed X-ray polarization is its prominent orbital-phase-dependent variation (Fig. 2). Interestingly, the polarization is mostly 'misaligned' from the east–west direction (from the orbital plane) during the phases of inferior and superior conjunctions when the left–right directions (which give non-zero contributions to the Stokes U) are expected to be symmetric in the simple picture with the cone-shaped funnel pointing in the direction of the orbital axis (see the orbital flux and PA profiles in Extended Data Fig. 7d–f). In the proposed scenario, the outflow from the compact object is expected to collide with the wind of the WR star, resulting in an asymmetry of the funnel and its surroundings.

We first considered geometries in which the funnel is an oblique, truncated cone. We also modelled a situation with the funnel axis not aligned with the orbital axis. In both cases, the orbital variations arose from the asymmetry of the funnel itself. The first model did not reproduce the strength of the signal in Stokes U because for a narrow funnel, most of the reflected photons that reach the observer are scattered at nearly the same angle, even for the additional part of the funnel surface producing geometrical asymmetry. The second case is reminiscent of the rotating vector model, for which there is a tight relation between the PD and PA variations[94,95]. To reproduce the phase shift between the observed PD and PA variations, the funnel had to be inclined in the direction of movement in the orbit. In contrast, a funnel moving through the stellar wind is expected to be tilted in the direction opposite to its velocity vector (at least, its optically thin outer parts, which contribute effectively to the observed emission and polarization). Hence, we conclude that the variations in U were not caused by the asymmetric shape of the funnel itself.

We also considered an alternative scenario in which the orbital modulation is produced by scattering of the primary X-ray emission at the point where the matter from the companion hits the accretion disk. This scenario for the orbital variability of Cyg X-3 system is analogous to low-mass X-ray binary systems at high inclinations[28]. The impact point contains heated material that can rise above the orbital plane to produce a regular attenuation or dipping pattern. The solid angle of this material is expected to be comparable to the size of the companion star, and the variations produced by this component are smaller than ~1% (for example, see the modelling and discussion in ref. 96). In contrast, an asymmetric structure with a substantial solid angle, as seen from the X-ray source, is required to reproduce the observed variations in the polarization.

The accretion geometry of Cyg X-3 and those of other high-mass X-ray binaries have a common component, the bow shock produced by the movement of the compact object through the wind of the companion. The outflow from the compact object is expected to collide with the wind of the WR star to produce an enhanced density region. The bow shock in Cyg X-3 has been exploited to explain the orbital changes of the X-ray and IR fluxes[22]. We tested to see whether this component could be responsible for the prominent polarimetric variations. In contrast to the beamed X-ray emission escaping along the funnel, the reflected and reprocessed light of the funnel walls is more isotropic. We suggest that the high-amplitude orbital variability of PA, as seen during both the Main and ToO observations, was produced thanks to the scattering of radiation reprocessed by the funnel walls from the inner surface of the bow shock. A fraction η_{bow} of the funnel radiation is scattered by the bow shock. We approximated its surface by a cylindrical sector parameterized by the angular extent ϕ_{cyl}, the azimuth of its centre at phase 0 (superior conjunction) relative to the line connecting the stars ϕ_{cen} and by the height-to-radius ratio of the cylinder H_{cyl}/ρ_{cyl}. In this combined geometry with the funnel and the bow shock, the average polarization comes from the radiation reflected from the funnel (described by the parameters α and R) and the orbital variability arises from the scattering of the mostly isotropic radiation off the inner surface of the bow shock (with parameters η_{bow}, ϕ_{cyl} and H_{cyl}/ρ_{cyl}). Note that the same geometry could also be applied to scenarios in which orbital variations are caused by scattering from the accretion stream or bulge. In that case, the scattering material should have a small azimuthal extent, $\phi_{cyl} < 90°$.

Extended Data Fig. 8 shows an example of orbital variations for parameters $\alpha = 10°$, $R = 50$, $H_{cyl}/\rho_{cyl} = 1$, $\phi_{cyl} = 220°$, $\phi_{cen} = 90°$ (at superior conjunction, the centre is to the left of the line connecting the stars) and $\eta_{bow} = 0.09$. We see, however, that the model does not reproduce the shape of the PD exactly, and we attribute this to the simplicity of the assumed bow shock geometry. For our parameter $\phi_{cen} = 90°$, the bow shock is at maximal angular distances from the plane formed by the observer, the WR star and the compact object at the superior and inferior conjunctions. In other words, we expect the PA to be a maximum or a minimum at the conjunctions and cross its average value, ~90°, close to quadratures. Because the PA was a maximum in the first orbital bin, we deduced that the Cyg X-3 system rotates in the anticlockwise direction.

Monte Carlo modelling of the toroidal envelope. To consider the effects of finite optical depth and the dependence of the resulting polarization on the geometry, we ran Monte Carlo simulations using the code STOKES v.2.07 (refs. 97,98). The code traces the polarization of photons propagating in media, taking into account the effects of photo-electric absorption and Compton downscattering. Both continuum and line emission are considered. Our goal was to identify the parameter space for which the average observed polarization can be reproduced. See ref. 99 for details of the modelling and for results for a broader parametric range and more distinct geometry cases. We show reprocessing for an elliptical torus (see Extended Data Fig. 10a for a geometry sketch), which represents an alternative geometry from the cone-shaped outflow that we described in the previous section (even though this geometry might not be directly applicable to the super-Eddington outflow configuration). The profile of the elliptical torus is parameterized through the cylindrical distance ρ, the grazing angle α, which is like the opening angle of the funnel in the cone geometry, and the minor axis b. Only the ratios of the distances affect the polarization properties. The point-like source at the centre of the coordinate system illuminates the axially symmetric scattering region.

The densities and atomic properties within the equatorial scattering region are homogeneous. The column density along the scatterer is proportional to the length of the scattering region between the source and the observer. We assumed the solar abundance from ref. 100 with $A_{Fe} = 1.0$, but we removed the neutral hydrogen from the absorbers due to the expected hydrogen-poor environment[16,19]. The main parameters of the medium that control the polarization properties are, thus, the neutral helium number density, which, being the most abundant element, is expressed through the column density N_{He} between the centre and an equatorial observer, and the number density of free electrons in the medium (related to ionization), defined through the equatorial electron-scattering Thomson optical depth τ_e. We show results for the unpolarized primary radiation but tested various cases of polarized primary emission[99]. The same holds for the primary spectral distribution, which we fix as a power law with the photon index $\Gamma = 3$ for simplicity.

As an example, Extended Data Fig. 10b shows the 2–8 keV integrated PD as a function of the observer inclination i and the ellipse grazing angle α for $N_{He} = 8.5 \times 10^{23}$ cm^{-2} and $\tau_e = 7$, corresponding to the partially ionized case with nearly equal number densities of helium and free electrons. The white dashed curves represent contours corresponding to PD ≈ 21 ± 3% in the 2–8 keV range, where the lower and upper limits correspond to the characteristic uncertainties of the simulations. Cells with a PD that fall in the correct range are highlighted with black rectangles. The contours form the same topology in the (i, α) space as for the analytical model and give similar, within uncertainties, allowed combinations of (i, α). We explored the parameter space with various aspect ratios and compared the multiple-scattering to single-scattering cases. In all cases, we were able to obtain a general pattern of two solutions, like the two branches in Fig. 4b. At 3.5–6 keV, we obtained almost no difference between the single-scattering and multiple-scattering cases, as at these energies, the single-scattering albedo is low. For all values of α and i in Extended Data Fig. 10b, the PA obtained was perpendicular to the axis of symmetry.

The energy dependence of polarization in the 2–8 keV range matches that of the Main observation if spectral lines are included[99]. If the density or ionization of the medium is lower, we obtain the same PA and lower PD, down to almost unpolarized emission, depending on the modelling subtleties. For an order-of-magnitude lower density, the results obtained are in line with the data in the ToO observation, supporting the interpretation of the decreased mass-accretion (and outflow) rate for this state.

Intrinsic and apparent luminosity estimates

Using the analytical model described above that was applied to the Main observation, we computed the luminosity escaping in the direction along the funnel axis L_{ULX} from the observed flux. We assumed that the primary X-ray source within the funnel is isotropic and produces luminosity L_X. In this case, the luminosity escaping in a given solid angle is proportional to this solid angle, $L_\Omega \propto \Omega$. Three distinct sites contribute to the total X-ray luminosity: the funnel opening, where the fraction proportional to the solid angle of the funnel escapes, the reprocessing site seen to the observer (region between point L and the upper boundary of the funnel in Extended Data Fig. 9a) and the lower layers of the funnel (between point L and the disk plane). The contribution of the latter luminosity may be in the form of soft reprocessed X-ray radiation and is not clearly visible in our data. The contribution of the former two can be related to the intrinsic X-ray luminosity:

$$L_{ULX} = \frac{2\pi}{\Omega_{ULX}} L_X, \tag{3}$$

where $\Omega_{ULX} = 2\pi(1 - \cos\alpha)$ is the solid angle of the funnel opening as seen from the primary X-ray source. The observer receives the flux F_{obs}, which is emitted by (reflected from) the visible part of the inner surface of the funnel (geometry in Extended Data Fig. 9a). The luminosity intercepted by this part can be expressed as

$$L_{refl} = \frac{\Omega_{refl}}{\Omega_{ULX}} a L_X, \tag{4}$$

where a is the scattering albedo and Ω_{refl} is the characteristic solid angle of the reflecting surface (which the observer is able to see), as viewed from the primary X-ray source. The reflected luminosity produces the observed flux we detect. Hence, $F_{obs} = L_{refl}/(4\pi D^2)$. Combining terms, we get an expression for the luminosity escaping along the funnel:

$$L_{ULX} = \frac{2\pi}{\Omega_{refl}} \frac{4\pi D^2 F_{obs}}{a}. \tag{5}$$

The solid angle of the reflecting surface can be expressed as

$$\frac{\Omega_{refl}}{2\pi} = \cos\alpha - \cos\alpha^*, \tag{6}$$

where α^* corresponds to the angle at which the lowest interior part of the funnel is seen by an observer (Extended Data Fig. 9). This angle is related to the funnel opening angle ζ as

$$\tan\alpha^* = \frac{\tan\zeta}{1 - 1/\rho_L}, \tag{7}$$

where ρ_L is the radius of the funnel at point L, in units of inner radii of the outflow. This radius can be expressed through the model parameter α, the cylindrical radius of the funnel outer boundary $\rho = R\sin\alpha$ and the observer inclination i as

$$\frac{1}{\rho_L} = \frac{1}{\rho}\frac{\tan i + \tan\zeta}{\tan i - \tan\zeta}. \tag{8}$$

The opening angle is, in turn, related to the model parameter α as

$$\tan\zeta = (1 - 1/\rho)\tan\alpha. \tag{9}$$

Substituting equations (8) and (9) into equation (7) and obtaining $\cos\alpha^*$, we find $\Omega_{refl}/2\pi$ as a function of the parameters ρ, α and i. Further, for the given observed polarization, we can relate α and R (see the red contour in Extended Data Fig. 9b), which makes $\Omega_{refl}/2\pi$ only a function of α. The solid red line in Extended Data Fig. 9c shows that, for all combinations (α, R) that give the observed polarization, $\Omega_{refl}/2\pi < 3 \times 10^{-2}$.

We take the observed flux (seen by IXPE, without correcting for the absorption in the WR wind and along the line of sight in the Galaxy) as a lower limit on $F_{obs} = 1.5 \times 10^{-9}$ erg cm^{-2} s^{-1} (which corresponds to the observed luminosity $L_{obs} = 1.6 \times 10^{37}$ erg s^{-1}, assuming the distance 9.7 kpc). Albedo is a function of energy, abundance and viewing angle[54]. Motivated by our spectral fitting (by comparing the intrinsic and reflected 2–8 keV spectra in Fig. 3), we take $a \approx 0.1$ as a conservative approximation. Inserting the numbers into equation (5), we get a lower limit on the luminosity seen along the funnel in the 2–8 keV range, $L_{ULX} = 5.5 \times 10^{39}$ erg s^{-1}.

To estimate the intrinsic X-ray luminosity, we need to take into account several additional factors. First, the observed fluxes have to be corrected for absorption. For our spectro-polarimetric modelling, however, we ignored absorption. Hence, we take $F_{unabs} = F_{obs}$. Further, we need to take into account the bolometric luminosity correction f_{bol}. This estimate consists of two contributions. First, the observed NICER flux (0.5–12 keV) is 1.7 times higher than the flux in the IXPE band (Table 1). Second, the higher-energy, 12–60 keV, part of the incident continuum contains luminosity that is 0.4 times that in the IXPE range, as computed from the spectral shape found in spectro-polarimetric fitting (Table 3). Hence, the lower-limit estimate on the flux in the 0.5–60 keV band is $2.1F_{obs}$. The lower-energy part of the spectrum would contribute more if the spectral peak were achieved at energies below IXPE band (which is, indeed, expected for the soft intrinsic spectrum). Hence, we put a conservative estimate on f_{bol} to be ≳ 2–3. Finally, we consider the range of luminosities for different pairs of (α, R) satisfying the observed PD (Extended Data Fig. 9). The intrinsic bolometric X-ray luminosity can be expressed through the unabsorbed X-ray flux as

$$L_{X,bol} = \frac{4\pi D^2 f_{bol} F_{unabs}}{a}\left(1 + \frac{\Omega_{ULX}}{\Omega_{refl}}\right) > 3 \times 10^{38}\left(1 + \frac{\Omega_{ULX}}{\Omega_{refl}}\right) \text{erg s}^{-1}. \tag{10}$$

The blue dashed line in Extended Data Fig. 9c shows the dependence of the amplification factor $(1 + \Omega_{ULX}/\Omega_{refl})$ on the angle α. The luminosity obtained can be compared to the Eddington luminosity for He (given

that the source shows hydrogen-poor properties[16]), so that $L_{\rm Edd,He} = 2.6 \times 10^{38} (M_{\rm X}/M_{\odot})$ erg s^{-1}, where $M_{\rm X}$ is the mass of the compact object and $M_{\odot}$ is the solar mass. For small funnel angles, $\alpha = 8°$, the intrinsic bolometric X-ray luminosity exceeds the Eddington limit for a compact object with low mass, $M_{\rm X}/M_{\odot} \lesssim 2$, such as a neutron star. Evolutionary arguments, however, suggest that the WR-fed compact object should swiftly become a black hole[101,102]. For a compact object $M_{\rm X}/M_{\odot} = 10$, we found that the bolometric luminosity estimate exceeds the Eddington limit (in He-rich material) for a combination of $\alpha = 15°$ and $f_{\rm bol} = 3$ or $\alpha = 16°$ and $f_{\rm bol} = 2$. For $\alpha > 16°$ and $f_{\rm bol} > 3$, the observed limit exceeds the Eddington limit for $M_{\rm X}/M_{\odot} = 20$, which corresponds to the heaviest Galactic black hole mass measured so far[103]. Interestingly, when scattering proceeds in the optically thin wind above the funnel, the factor in brackets should be replaced with $1/\tau_{\rm T,WR} \approx 2$–10, which does not affect the final estimate of the intrinsic luminosity.

If the source is surrounded by an envelope with a narrow funnel, the primary luminosity will be beamed in the direction along its axis[36]. From the constraints obtained for the funnel half-opening angle $\zeta (\lesssim \alpha)$, we can directly get the geometrical amplification (beaming) factor,

$$b = \frac{1}{1 - \cos\zeta} \gtrsim 30. \tag{11}$$

The beaming is expected to vary with the opening angle and may ultimately depend on the mass-accretion rate[37]. More precise estimates of the beaming factor may be obtained by taking into account the interactions of photons with the funnel walls[104,105]. Monte Carlo simulations of multiple reflection and reprocessing events within the funnel show that a substantial fraction of photons leave the system outside the solid angle $\Omega_{\rm ULX}$, leading to a reduction of the beaming factor. The magnitude of the reduction, in turn, depends on the height of the funnel. More photons leave the system outside $\Omega_{\rm ULX}$ for larger R. The estimate in equation (11) corresponds to the limiting case of infinitely large R.

Data availability

The IXPE, NuSTAR, NICER, INTEGRAL and Fermi data are freely available in the HEASARC Data Archive (https://heasarc.gsfc.nasa.gov). The SRG ART-XC data are available via ftp://hea.iki.rssi.ru/public/SRG/ART-XC/data/Cyg_X-3/artxc_cygx3_04-20keV_lcurve.qdp. The multiwavelength raw data are available on request from the individual observatories.

Code availability

The analysis and simulation software IXPEOBSSIM developed by the IXPE Collaboration and its documentation is available publicly through the web-page https://ixpeobssim.readthedocs.io/en/latest/?badge=latest.494. XSPEC is distributed and maintained under the aegis of the HEASARC and can be downloaded as part of HEAsoft from http://heasarc.gsfc.nasa.gov/docs/software/lheasoft/download.html. The MIR software package for the SMA data is available at https://lweb.cfa.harvard.edu/~cqi/mircook.html. Models of the polarized emission from the funnel are available via Zenodo at https://zenodo.org/records/10889892 (ref. 106). The STOKES code v.2.07 is available upon reasonable request from the authors.

References

1. Giacconi, R., Gorenstein, P., Gursky, H. & Waters, J. R. An X-ray survey of the Cygnus region. *Astrophys. J.* **148**, L119–L127 (1967).
2. Gregory, P. C. & Kronberg, P. P. Discovery of giant radio outburst from Cygnus X-3. *Nature* **239**, 440–443 (1972).
3. McCollough, M. L. et al. Discovery of correlated behavior between the hard X-ray and the radio bands in Cygnus X-3. *Astrophys. J.* **517**, 951–955 (1999).
4. Corbel, S. et al. A giant radio flare from Cygnus X-3 with associated γ-ray emission. *Mon. Not. R. Astron. Soc.* **421**, 2947–2955 (2012).
5. Atwood, W. B. et al. The large area telescope on the Fermi Gamma-Ray Space Telescope mission. *Astrophys. J.* **697**, 1071–1102 (2009).
6. Tavani, M. et al. Extreme particle acceleration in the microquasar Cygnus X-3. *Nature* **462**, 620–623 (2009).
7. Lommen, D., Yungelson, L., van den Heuvel, E., Nelemans, G. & Portegies Zwart, S. Cygnus X-3 and the problem of the missing Wolf–Rayet X-ray binaries. *Astron. Astrophys.* **443**, 231–241 (2005).
8. Belczynski, K. et al. Cyg X-3: a Galactic double black hole or black-hole-neutron-star progenitor. *Astrophys. J.* **764**, 96 (2013).
9. van Kerkwijk, M. H. et al. Infrared helium emission lines from Cygnus X-3 suggesting a Wolf–Rayet star companion. *Nature* **355**, 703–705 (1992).
10. van Kerkwijk, M. H., Geballe, T. R., King, D. L., van der Klis, M. & van Paradijs, J. The Wolf–Rayet counterpart of Cygnus X-3. *Astron. Astrophys.* **314**, 521–540 (1996).
11. Reid, M. J. & Miller-Jones, J. C. A. On the distances to the X-ray binaries Cygnus X-3 and GRS 1915+105. *Astrophys. J.* **959**, 85 (2023).
12. McCollough, M. L., Corrales, L. & Dunham, M. M. Cygnus X-3: its little friend's counterpart, the distance to Cygnus X-3, and outflows/jets. *Astrophys. J. Lett.* **830**, 36 (2016).
13. Martí, J., Paredes, J. M. & Peracaula, M. The Cygnus X-3 radio jets at arcsecond scales. *Astrophys. J.* **545**, 939–944 (2000).
14. Miller-Jones, J. C. A. et al. Time-sequenced multi-radio frequency observations of Cygnus X-3 in flare. *Astrophys. J.* **600**, 368–389 (2004).
15. Jones, T. J., Gehrz, R. D., Kobulnicky, H. A., Molnar, L. A. & Howard, E. M. Infrared photometry and polarimetry of Cygnus X-3. *Astron. J.* **108**, 605–611 (1994).
16. Fender, R. P., Hanson, M. M. & Pooley, G. G. Infrared spectroscopic variability of Cygnus X-3 in outburst and quiescence. *Mon. Not. R. Astron. Soc.* **308**, 473–484 (1999).
17. Hjellming, R. M. An astronomical puzzle called Cygnus X-3. *Science* **182**, 1089–1095 (1973).
18. Vilhu, O., Hakala, P., Hannikainen, D. C., McCollough, M. & Koljonen, K. Orbital modulation of X-ray emission lines in Cygnus X-3. *Astron. Astrophys.* **501**, 679–686 (2009).
19. Kallman, T. et al. Photoionization emission models for the Cyg X-3 X-ray spectrum. *Astrophys. J.* **874**, 51 (2019).
20. van der Klis, M. & Bonnet-Bidaud, J. M. A change in light curve asymmetry and the ephemeris of CYG X-3. *Astron. Astrophys.* **95**, 5–7 (1981).
21. Antokhin, I. I. & Cherepashchuk, A. M. The period change of Cyg X-3. *Astrophys. J.* **871**, 244 (2019).
22. Antokhin, I. I., Cherepashchuk, A. M., Antokhina, E. A. & Tatarnikov, A. M. Near-IR and X-ray variability of Cyg X-3: evidence for a compact IR source and complex wind structures. *Astrophys. J.* **926**, 123 (2022).
23. Mioduszewski, A. J., Rupen, M. P., Hjellming, R. M., Pooley, G. G. & Waltman, E. B. A one-sided highly relativistic jet from Cygnus X-3. *Astrophys. J.* **553**, 766–775 (2001).
24. Szostek, A., Zdziarski, A. A. & McCollough, M. L. A classification of the X-ray and radio states of Cyg X-3 and their long-term correlations. *Mon. Not. R. Astron. Soc.* **388**, 1001–1010 (2008).
25. Zdziarski, A. A., Misra, R. & Gierliński, M. Compton scattering as the explanation of the peculiar X-ray properties of Cyg X-3. *Mon. Not. R. Astron. Soc.* **402**, 767–775 (2010).
26. Hjalmarsdotter, L. et al. The nature of the hard state of Cygnus X-3. *Mon. Not. R. Astron. Soc.* **384**, 278–290 (2008).
27. Milgrom, M. & Pines, D. Cygnus X-3: a cocooned X-ray binary pulsar? *Astrophys. J.* **220**, 272–278 (1978).
28. White, N. E. & Holt, S. S. Accretion disk coronae. *Astrophys. J.* **257**, 318–337 (1982).

29. Weisskopf, M. C. et al. The Imaging X-Ray Polarimetry Explorer (IXPE): pre-launch. *J. Astron. Telesc. Instrum. Syst.* **8**, 026002 (2022).
30. Brown, J. C., McLean, I. S. & Emslie, A. G. Polarisation by Thomson scattering in optically thin stellar envelopes. II. Binary and multiple star envelopes and the determination of binary inclinations. *Astron. Astrophys.* **68**, 415–427 (1978).
31. Ursini, F. et al. Mapping the circumnuclear regions of the Circinus galaxy with the Imaging X-ray Polarimetry Explorer. *Mon. Not. R. Astron. Soc.* **519**, 50–58 (2023).
32. Shakura, N. I. & Sunyaev, R. A. Black holes in binary systems. Observational appearance. *Astron. Astrophys.* **24**, 337–355 (1973).
33. Poutanen, J., Lipunova, G., Fabrika, S., Butkevich, A. G. & Abolmasov, P. Supercritically accreting stellar mass black holes as ultraluminous X-ray sources. *Mon. Not. R. Astron. Soc.* **377**, 1187–1194 (2007).
34. Sądowski, A., Narayan, R., McKinney, J. C. & Tchekhovskoy, A. Numerical simulations of super-critical black hole accretion flows in general relativity. *Mon. Not. R. Astron. Soc.* **439**, 503–520 (2014).
35. Kaaret, P., Feng, H. & Roberts, T. P. Ultraluminous X-ray sources. *Annu. Rev. Astron. Astrophys.* **55**, 303–341 (2017).
36. King, A. R., Davies, M. B., Ward, M. J., Fabbiano, G. & Elvis, M. Ultraluminous X-ray sources in external galaxies. *Astrophys. J. Lett.* **552**, 109–112 (2001).
37. King, A. R. Masses, beaming and Eddington ratios in ultraluminous X-ray sources. *Mon. Not. R. Astron. Soc.* **393**, 41–44 (2009).
38. Middleton, M. J. et al. NuSTAR reveals the hidden nature of SS433. *Mon. Not. R. Astron. Soc.* **506**, 1045–1058 (2021).
39. Fabrika, S. The jets and supercritical accretion disk in SS433. *Astrophys. Space Phys. Rev.* **12**, 1–152 (2004).
40. Done, C., Wardziński, G. & Gierliński, M. GRS 1915+105: the brightest Galactic black hole. *Mon. Not. R. Astron. Soc.* **349**, 393–403 (2004).
41. Casares, J. & Jonker, P. G. Mass measurements of stellar and intermediate-mass black holes. *Space Sci. Rev.* **183**, 223–252 (2014).
42. Motta, S. E. et al. Swift observations of V404 Cyg during the 2015 outburst: X-ray outflows from super-Eddington accretion. *Mon. Not. R. Astron. Soc.* **471**, 1797–1818 (2017).
43. Revnivtsev, M., Sunyaev, R., Gilfanov, M. & Churazov, E. V4641Sgr – a super-Eddington source enshrouded by an extended envelope. *Astron. Astrophys.* **385**, 904–908 (2002).
44. MacDonald, R. K. D. et al. The black hole binary V4641 Sagitarii: activity in quiescence and improved mass determinations. *Astrophys. J.* **784**, 2 (2014).
45. Long, K. S., Chanan, G. A. & Novick, R. The X-ray polarization of the Cygnus sources. *Astrophys. J.* **238**, 710–716 (1980).
46. Krawczynski, H. et al. Polarized X-rays constrain the disk-jet geometry in the black hole X-ray binary Cygnus X-1. *Science* **378**, 650–654 (2022).
47. Di Marco, A. et al. Handling the background in IXPE polarimetric data. *Astron. J.* **165**, 143 (2023).
48. Strohmayer, T. E. X-ray spectro-polarimetry with photoelectric polarimeters. *Astrophys. J.* **838**, 72 (2017).
49. Arnaud, K. A. in *Astronomical Data Analysis Software and Systems V* (eds Jacoby, G. H. and Barnes, J.) 17 (ASP, 1996).
50. Baldini, L. et al. ixpeobssim: a simulation and analysis framework for the Imaging X-ray Polarimetry Explorer. *SoftwareX* **19**, 101194 (2022).
51. Kislat, F., Clark, B., Beilicke, M. & Krawczynski, H. Analyzing the data from X-ray polarimeters with Stokes parameters. *Astropart. Phys.* **68**, 45–51 (2015).
52. Harrison, F. A. et al. The Nuclear Spectroscopic Telescope Array (NuSTAR) high-energy X-ray mission. *Astrophys. J.* **770**, 103 (2013).
53. Madsen, K. K., Forster, K., Grefenstette, B., Harrison, F. A. & Miyasaka, H. Effective area calibration of the Nuclear Spectroscopic Telescope Array. *J. Astron. Telesc. Instrum. Syst.* **8**, 034003 (2022).
54. Magdziarz, P. & Zdziarski, A. A. Angle-dependent Compton reflection of X-rays and gamma-rays. *Mon. Not. R. Astron. Soc.* **273**, 837–848 (1995).
55. Zdziarski, A. A., Johnson, W. N. & Magdziarz, P. Broad-band γ-ray and X-ray spectra of NGC 4151 and their implications for physical processes and geometry. *Mon. Not. R. Astron. Soc.* **283**, 193–206 (1996).
56. Fabrika, S. N., Atapin, K. E., Vinokurov, A. S. & Sholukhova, O. N. Ultraluminous X-ray sources. *Astrophys. Bull.* **76**, 6–38 (2021).
57. King, A., Lasota, J.-P. & Middleton, M. Ultraluminous X-ray sources. *New Astron. Rev.* **96**, 101672 (2023).
58. Koljonen, K. I. I., Hannikainen, D. C., McCollough, M. L., Pooley, G. G. & Trushkin, S. A. The hardness–intensity diagram of Cygnus X-3: revisiting the radio/X-ray states. *Mon. Not. R. Astron. Soc.* **406**, 307–319 (2010).
59. Zdziarski, A. A., Mikolajewska, J. & Belczynski, K. Cyg X-3: a low-mass black hole or a neutron star. *Mon. Not. R. Astron. Soc.* **429**, 104–108 (2013).
60. Koljonen, K. I. I. & Maccarone, T. J. Gemini/GNIRS infrared spectroscopy of the Wolf–Rayet stellar wind in Cygnus X-3. *Mon. Not. R. Astron. Soc.* **472**, 2181–2195 (2017).
61. Suryanarayanan, A., Paerels, F. & Leutenegger, M. The high resolution Fe K spectrum of Cygnus X-3. Preprint at https://arxiv.org/abs/2212.04165 (2022).
62. Egron, E. et al. Investigating the mini and giant radio flare episodes of Cygnus X-3. *Astrophys. J.* **906**, 10 (2021).
63. Parsignault, D. R. et al. Observations of Cygnus X-3 by Uhuru. *Nat. Phys. Sci.* **239**, 123–125 (1972).
64. Bonnet-Bidaud, J. M. & van der Klis, M. The X-ray modulation of CYG X-3. *Astron. Astrophys.* **101**, 299–304 (1981).
65. Mason, K. O., Cordova, F. A. & White, N. E. Simultaneous X-ray and infrared observations of Cygnus X-3. *Astrophys. J.* **309**, 700–706 (1986).
66. Zdziarski, A. A. et al. A comprehensive study of high-energy gamma-ray and radio emission from Cyg X-3. *Mon. Not. R. Astron. Soc.* **479**, 4399–4415 (2018).
67. Stark, M. J. & Saia, M. Doppler modulation of X-ray lines in Cygnus X-3. *Astrophys. J. Lett.* **587**, 101–104 (2003).
68. Zdziarski, A. A., Maitra, C., Frankowski, A., Skinner, G. K. & Misra, R. Energy-dependent orbital modulation of X-rays and constraints on emission of the jet in Cyg X-3. *Mon. Not. R. Astron. Soc.* **426**, 1031–1042 (2012).
69. Willingale, R., King, A. R. & Pounds, K. A. EXOSAT MEDA observations of Cygnus X-3. *Mon. Not. R. Astron. Soc.* **215**, 295–314 (1985).
70. Poutanen, J., Nagendra, K. N. & Svensson, R. Green's matrix for Compton reflection of polarized radiation from cold matter. *Mon. Not. R. Astron. Soc.* **283**, 892–904 (1996).
71. Axelsson, M., Larsson, S. & Hjalmarsdotter, L. The aperiodic broad-band X-ray variability of Cygnus X-3. *Mon. Not. R. Astron. Soc.* **394**, 1544–1550 (2009).
72. Sunyaev, R. et al. SRG X-ray orbital observatory. Its telescopes and first scientific results. *Astron. Astrophys.* **656**, A132 (2021).
73. Pavlinsky, M. et al. The ART-XC telescope on board the SRG observatory. *Astron. Astrophys.* **650**, A42 (2021).
74. Ubertini, P. et al. Bursts from GS 1826-238: a clocked thermonuclear flashes generator. *Astrophys. J. Lett.* **514**, 27–30 (1999).
75. Lebrun, F. et al. ISGRI: the INTEGRAL soft gamma-ray imager. *Astron. Astrophys.* **411**, 141–148 (2003).
76. Courvoisier, T. J.-L. et al. The INTEGRAL Science Data Centre (ISDC). *Astron. Astrophys.* **411**, 53–57 (2003).

77. Neronov, A. et al. Online data analysis system of the INTEGRAL telescope. *Astron. Astrophys.* **651**, A97 (2021).
78. Mattox, J. R. et al. The likelihood analysis of EGRET data. *Astrophys. J.* **461**, 396–407 (1996).
79. Atwood, W. et al. Pass 8: toward the full realization of the Fermi-LAT scientific potential. Preprint at https://arxiv.org/abs/1303.3514 (2013).
80. Abdollahi, S. et al. Fermi Large Area Telescope Fourth Source Catalog. *Astrophys. J. Suppl. Ser.* **247**, 33 (2020).
81. Tavani, M. et al. The AGILE Mission. *Astron. Astrophys.* **502**, 995–1013 (2009).
82. Pittori, C. The AGILE data center and its legacy. *Rend. Lincei Sci. Fis. Nat.* **30**, 217–223 (2019).
83. Bulgarelli, A. et al. Evaluating the maximum likelihood method for detecting short-term variability of AGILE γ-ray sources. *Astron. Astrophys.* **540**, A79 (2012).
84. Bulgarelli, A. et al. Second AGILE catalogue of gamma-ray sources. *Astron. Astrophys.* **627**, A13 (2019).
85. Zwart, J. T. L. et al. The Arcminute Microkelvin Imager. *Mon. Not. R. Astron. Soc.* **391**, 1545–1558 (2008).
86. Hickish, J. et al. A digital correlator upgrade for the Arcminute MicroKelvin Imager. *Mon. Not. R. Astron. Soc.* **475**, 5677–5687 (2018).
87. Ott, M. et al. An updated list of radio flux density calibrators. *Astron. Astrophys.* **284**, 331–339 (1994).
88. Egron, E. et al. Single-dish and VLBI observations of Cygnus X-3 during the 2016 giant flare episode. *Mon. Not. R. Astron. Soc.* **471**, 2703–2714 (2017).
89. Trushkin, S. A. et al. Study of the microquasar Cygnus X-3 with the RATAN-600 Radio Telescope in multi-azimuth observing mode. *Astrophys. Bull.* **78**, 225–233 (2023).
90. Tsybulev, P. G. et al. C-band radiometer for continuum observations at RATAN-600 Radio Telescope. *Astrophys. Bull.* **73**, 494–500 (2018).
91. Kale, R. & Ishwara-Chandra, C. H. CAPTURE: a continuum imaging pipeline for the uGMRT. *Exp. Astron.* **51**, 95–108 (2021).
92. Marrone, D. P. & Rao, R. The submillimeter array polarimeter. In *Proc. Millimeter and Submillimeter Detectors and Instrumentation for Astronomy IV* Vol. 7020 (eds Duncan, W. D. et al.) 70202B (SPIE, 2008).
93. Chandrasekhar, S. *Radiative Transfer* (Dover, 1960).
94. Radhakrishnan, V. & Cooke, D. J. Magnetic poles and the polarization structure of pulsar radiation. *Astrophys. Lett.* **3**, 225–229 (1969).
95. Poutanen, J. Relativistic rotating vector model for X-ray millisecond pulsars. *Astron. Astrophys.* **641**, A166 (2020).
96. Rankin, J. et al. X-ray polarimetry as a tool to constrain orbital parameters in X-ray binaries. *Astrophys. J.* **962**, 34 (2024).
97. Goosmann, R. W. & Gaskell, C. M. Modeling optical and UV polarization of AGNs. I. Imprints of individual scattering regions. *Astron. Astrophys.* **465**, 129–145 (2007).
98. Marin, F., Dovčiak, M., Muleri, F., Kislat, F. F. & Krawczynski, H. S. Predicting the X-ray polarization of type 2 Seyfert galaxies. *Mon. Not. R. Astron. Soc.* **473**, 1286–1316 (2018).
99. Podgorný, J., Marin, F. & Dovčiak, M. X-ray polarization properties of partially ionized equatorial obscurers around accreting compact objects. *Mon. Not. R. Astron. Soc.* **526**, 4929–4951 (2023).
100. Asplund, M., Grevesse, N. & Sauval, A. J. The solar chemical composition. In *Proc. Cosmic Abundances as Records of Stellar Evolution and Nucleosynthesis* (eds Barnes, T. G. III & Bash, F. N.) 25 (ASP, 2005).
101. Lipunov, V. M. Why are no X-ray pulsars paired with Wolf–Rayet stars? *Sov. Astron. Lett.* **8**, 194–196 (1982).
102. Bogomazov, A. I. A study of the evolution of the close binaries Cyg X-3, IC 10 X-1, NGC 300 X-1, SS 433, and M33 X-7 using the 'scenario machine'. *Astron. Rep.* **58**, 126–138 (2014).
103. Miller-Jones, J. C. A. et al. Cygnus X-1 contains a 21-solar mass black hole—Implications for massive star winds. *Science* **371**, 1046–1049 (2021).
104. Dauser, T., Middleton, M. & Wilms, J. Modelling the light curves of ultraluminous X-ray sources as precession. *Mon. Not. R. Astron. Soc.* **466**, 2236–2241 (2017).
105. Mushtukov, A. A. & Portegies Zwart, S. Bright X-ray pulsars: how outflows influence beaming, pulsations and pulse phase lags. *Mon. Not. R. Astron. Soc.* **518**, 5457–5464 (2023).
106. Poutanen, J. Polarization properties of radiation scattered from a frustrum surface. *Zenodo* https://zenodo.org/records/10889892 (2024).
107. Zdziarski, A. A., Segreto, A. & Pooley, G. G. The radio/X-ray correlation in Cyg X-3 and the nature of its hard spectral state. *Mon. Not. R. Astron. Soc.* **456**, 775–789 (2016).

Acknowledgements

IXPE is a joint US and Italian mission. The US contribution is supported by the National Aeronautics and Space Administration (NASA) and led and managed by its Marshall Space Flight Center, with industry partner Ball Aerospace (Contract NNM15AA18C). The Italian contribution is supported by ASI (Contract ASI-OHBI-2017-12-I.0 and Agreements ASI-INAF-2017-12-H0 and ASI-INFN-2017.13-H0) and its Space Science Data Center and by the Italian National Institute for Astrophysics and the Italian National Institute for Nuclear Physics. For the AMI observations, we thank the staff of the Mullard Radio Astronomy Observatory, University of Cambridge, for their support in the maintenance and operation of the telescope, and we acknowledge support from the European Research Council (Grant No. ERC-2012-StG-307215 LODESTONE). The SMA is a joint project between the Smithsonian Astrophysical Observatory and the Academia Sinica Institute of Astronomy and Astrophysics and is funded by the Smithsonian Institution and the Academia Sinica. SMA is on Maunakea, which is a culturally important site for the indigenous Hawaiian people; we are privileged to study the cosmos from its summit. This work is partly based on observations with the 100-m telescope of the Max Planck Institute for Radio Astronomy at Effelsberg. The research leading to these results has received funding from the European Union's Horizon 2020 research and innovation programme (Grant Agreement No. 101004719; ORP). The AGILE Mission is funded by ASI with scientific and programmatic participation by the Italian National Institute for Astrophysics and the Italian National Institute for Nuclear Physics. This investigation was supported by the ASI (Grant No. I/028/12/7-2022). We thank H. Feng for providing the data on the representative ULX models. F. Muleri, A.D.M., F.L.M., E. Costa, P. Soffitta, S.F. and R.F. are partially supported by the Italian Ministry of Foreign Affairs (Grant No. CN24GR08, GRBAXP: Guangxi-Rome Bilateral Agreement for X-ray Polarimetry in Astrophysics). A.V., J. Poutanen and S.S.T. acknowledge support from the Academy of Finland (Grant Nos. 333112, 347003, 349144, 349373, 349906 and 355672). A.A.M. is supported by the Stephen Hawking fellowship from UK Research and Innovation. H.K. and N.R.C. acknowledge NASA support (Grant Nos. 80NSSC18K0264, 80NSSC22K1291, 80NSSC21K1817 and NNX16AC42G). V.D. thanks the German Academic Exchange Service (Travel Grant No. 57525212). A.I. acknowledges support from the Royal Society. J. Podgorný, M.D., J.S. and V.K. give thanks for support from the Czech Science Foundation (Project 21-06825X) and institutional support from the Astronomical Institute of the Czech Academy of Sciences (Project RVO:67985815). We thank the staff of the GMRT who made these observations possible. GMRT is run by the National Centre for Radio Astrophysics of the Tata Institute of Fundamental Research. R.K. acknowledges the support of the Department of Atomic Energy, Government of India (Project No. 12-R&D-TFR-5.02-0700). M.M. is supported by NASA (Contract NAS8-03060). S.A.T. is supported

by the Ministry of Science and Higher Education of the Russian Federation (Grant No. 075-15-2022-262; 13.MNPMU.21.0003). A.A.Z. acknowledges support from the Polish National Science Center (Grant No. 2019/35/B/ST9/03944).

Author contributions

A.V. led the modelling of the data and the writing of the paper. F. Muleri led the analysis of the IXPE data. J. Poutanen led the analytical modelling and contributed to the writing of the paper. J. Podgorný performed the Monte Carlo simulations in support of the modelling. M.D. led the work of the IXPE Topical Working Group on Accreting Stellar-mass Black Holes. A.D.R., E. Churazov, P.K. and R.A.S. contributed with parts of the paper and its content. F.C., A.D.M., S.V.F., H.K., F.L.M., A.A.L., S.V.M., A.R., N.R.C., J.F.S., S.S.T., A.A.Z. and J.J.E.K., I.A.M., G.P. and C.P. contributed to planning, reducing and analysing the X-ray and γ-ray data. V.L., A.A.M. and D.M. contributed to analytical estimates and modelling. J.S.B., N. Bursov, E.E., D.A.G., M.G., R.K., A.K., M.M., N.N., M. Pilia, R.R., S.R., A.S., J.S., S.A.T. and P.T. contributed with radio and submillimetre data. S.B., E. Costa, J.A.G., A.I., F. Marin, G.M., P. Soffitta, F. Tombesi, F.U., M.C.W. and K.W. contributed with discussions of the methods and conclusions. The remaining authors contributed to the design, science case of the IXPE mission and the planning of observations relevant to the present paper.

Competing interests

The authors declare no competing interests.

Additional information

Extended data is available for this paper at https://doi.org/10.1038/s41550-024-02294-9.

Correspondence and requests for materials should be addressed to Alexandra Veledina.

Peer review information *Nature Astronomy* thanks Nicholas White and the other, anonymous, reviewer(s) for their contribution to the peer review of this work.

Reprints and permissions information is available at www.nature.com/reprints.

Publisher's note Springer Nature remains neutral with regard to jurisdictional claims in published maps and institutional affiliations.

Alexandra Veledina[1,2] ✉, Fabio Muleri[3], Juri Poutanen[1], Jakub Podgorný[4,5,6], Michal Dovčiak[5], Fiamma Capitanio[3], Eugene Churazov[7], Alessandra De Rosa[3], Alessandro Di Marco[3], Sofia V. Forsblom[1], Philip Kaaret[8], Henric Krawczynski[9], Fabio La Monaca[3,10,11], Vladislav Loktev[1], Alexander A. Lutovinov[65], Sergey V. Molkov[65], Alexander A. Mushtukov[12], Ajay Ratheesh[3], Nicole Rodriguez Cavero[9], James F. Steiner[13], Rashid A. Sunyaev[7], Sergey S. Tsygankov[1], Martin C. Weisskopf[8], Andrzej A. Zdziarski[14], Stefano Bianchi[15], Joe S. Bright[12], Nikolaj Bursov[16], Enrico Costa[3], Elise Egron[17], Javier A. Garcia[18,19], David A. Green[20], Mark Gurwell[13], Adam Ingram[21], Jari J. E. Kajava[1,22], Ruta Kale[23], Alex Kraus[24], Denys Malyshev[25], Frédéric Marin[4], Giorgio Matt[15], Michael McCollough[13], Ilya A. Mereminskiy[65], Nikolaj Nizhelsky[16], Giovanni Piano[3], Maura Pilia[17], Carlotta Pittori[26,27], Ramprasad Rao[13], Simona Righini[28], Paolo Soffitta[3], Anton Shevchenko[16], Jiri Svoboda[5], Francesco Tombesi[10,29,30], Sergei A. Trushkin[16,31], Peter Tsybulev[16], Francesco Ursini[15], Kinwah Wu[32], Iván Agudo[33], Lucio A. Antonelli[26,27], Matteo Bachetti[17], Luca Baldini[34,35], Wayne H. Baumgartner[8], Ronaldo Bellazzini[34], Stephen D. Bongiorno[8], Raffaella Bonino[36,37], Alessandro Brez[33], Niccolò Bucciantini[38,39,40], Simone Castellano[34], Elisabetta Cavazzuti[41], Chien-Ting Chen[42], Stefano Ciprini[26,29], Ettore Del Monte[3], Laura Di Gesu[41], Niccolò Di Lalla[43], Immacolata Donnarumma[41], Victor Doroshenko[25], Steven R. Ehlert[8], Teruaki Enoto[44], Yuri Evangelista[3], Sergio Fabiani[3], Riccardo Ferrazzoli[3], Shuichi Gunji[45], Kiyoshi Hayashida[46], Jeremy Heyl[47], Wataru Iwakiri[48], Svetlana G. Jorstad[49,50], Vladimir Karas[5], Fabian Kislat[51], Takao Kitaguchi[44], Jeffery J. Kolodziejczak[8], Luca Latronico[36], Ioannis Liodakis[52], Simone Maldera[36], Alberto Manfreda[34], Andrea Marinucci[41], Alan P. Marscher[49], Herman L. Marshall[53], Francesco Massaro[36,37], Ikuyuki Mitsuishi[54], Tsunefumi Mizuno[55], Michela Negro[18,56,57], Chi-Yung Ng[58], Stephen L. O'Dell[8], Nicola Omodei[43], Chiara Oppedisano[36], Alessandro Papitto[27], George G. Pavlov[59], Abel L. Peirson[43], Matteo Perri[26,27], Melissa Pesce-Rollins[34], Pierre-Olivier Petrucci[60], Andrea Possenti[17], Simonetta Puccetti[26], Brian D. Ramsey[8], John Rankin[3], Oliver Roberts[42], Roger W. Romani[43], Carmelo Sgrò[34], Patrick Slane[13], Gloria Spandre[34], Doug Swartz[42], Toru Tamagawa[44], Fabrizio Tavecchio[61], Roberto Taverna[62], Yuzuru Tawara[54], Allyn F. Tennant[8], Nicholas E. Thomas[8], Alessio Trois[17], Roberto Turolla[32,62], Jacco Vink[63], Fei Xie[3,64] & Silvia Zane[32]

[1]Department of Physics and Astronomy, University of Turku, Turku, Finland. [2]Nordita, KTH Royal Institute of Technology and Stockholm University, Stockholm, Sweden. [3]INAF Istituto di Astrofisica e Planetologia Spaziali, Rome, Italy. [4]Université de Strasbourg, CNRS, Observatoire Astronomique de Strasbourg, Strasbourg, France. [5]Astronomical Institute of the Czech Academy of Sciences, Prague, Czech Republic. [6]Astronomical Institute, Charles University, Prague, Czech Republic. [7]Max Planck Institute for Astrophysics, Garching, Germany. [8]NASA Marshall Space Flight Center, Hunt sville, AL, USA. [9]Physics Department and McDonnell Center for the Space Sciences, Washington University in St Louis, St Louis, MO, USA. [10]Dipartimento di Fisica, Università degli Studi di Roma 'Tor Vergata', Rome, Italy. [11]Dipartimento di Fisica, Università degli Studi di Roma 'La Sapienza', Rome, Italy. [12]Astrophysics,

Department of Physics, University of Oxford, Oxford, UK. [13]Harvard-Smithsonian Center for Astrophysics, Cambridge, MA, USA. [14]Nicolaus Copernicus Astronomical Center, Polish Academy of Sciences, Warsaw, Poland. [15]Dipartimento di Matematica e Fisica, Università degli Studi Roma Tre, Rome, Italy. [16]Special Astrophysical Observatory of the Russian Academy of Sciences, Nizhnij Arkhyz, Russia. [17]INAF Osservatorio Astronomico di Cagliari, Selargius, Italy. [18]NASA Goddard Space Flight Center, Greenbelt, MD, USA. [19]California Institute of Technology, Pasadena, CA, USA. [20]Cavendish Laboratory, University of Cambridge, Cambridge, UK. [21]School of Mathematics, Statistics, and Physics, Newcastle University, Newcastle upon Tyne, UK. [22]Serco for the European Space Agency (ESA), European Space Astronomy Centre, Madrid, Spain. [23]National Centre for Radio Astrophysics, Tata Institute of Fundamental Research, Pune, India. [24]Max-Planck-Institut für Radioastronomie, Bonn, Germany. [25]Institut für Astronomie und Astrophysik, Universität Tübingen, Tübingen, Germany. [26]Space Science Data Center, Agenzia Spaziale Italiana, Rome, Italy. [27]INAF Osservatorio Astronomico di Roma, Rome, Italy. [28]INAF Institute of Radio Astronomy, Bologna, Italy. [29]Istituto Nazionale di Fisica Nucleare, Sezione di Roma 'Tor Vergata', Rome, Italy. [30]Department of Astronomy, University of Maryland, College Park, MD, USA. [31]Kazan Federal University, Kazan, Russia. [32]Mullard Space Science Laboratory, University College London, Dorking, UK. [33]Instituto de Astrofísica de Andalucía–CSIC, Granada, Spain. [34]Istituto Nazionale di Fisica Nucleare, Sezione di Pisa, Pisa, Italy. [35]Dipartimento di Fisica, Università di Pisa, Pisa, Italy. [36]Istituto Nazionale di Fisica Nucleare, Sezione di Torino, Turin, Italy. [37]Dipartimento di Fisica, Università degli Studi di Torino, Turin, Italy. [38]INAF Osservatorio Astrofisico di Arcetri, Florence, Italy. [39]Dipartimento di Fisica e Astronomia, Università degli Studi di Firenze, Florence, Italy. [40]Istituto Nazionale di Fisica Nucleare, Sezione di Firenze, Florence, Italy. [41]Agenzia Spaziale Italiana, Rome, Italy. [42]Science and Technology Institute, Universities Space Research Association, Huntsville, AL, USA. [43]Department of Physics and Kavli Institute for Particle Astrophysics and Cosmology, Stanford University, Stanford, CA, USA. [44]RIKEN Cluster for Pioneering Research, Wako, Japan. [45]Yamagata University, Yamagata-shi, Japan. [46]Osaka University, Suita, Japan. [47]University of British Columbia, Vancouver, British Columbia, Canada. [48]International Center for Hadron Astrophysics, Chiba University, Chiba, Japan. [49]Institute for Astrophysical Research, Boston University, Boston, MA, USA. [50]Department of Astrophysics, St Petersburg State University, St Petersburg, Russia. [51]Department of Physics and Astronomy and Space Science Center, University of New Hampshire, Durham, NH, USA. [52]Finnish Centre for Astronomy with ESO, University of Turku, Turku, Finland. [53]MIT Kavli Institute for Astrophysics and Space Research, Massachusetts Institute of Technology, Cambridge, MA, USA. [54]Graduate School of Science, Division of Particle and Astrophysical Science, Nagoya University, Nagoya, Japan. [55]Hiroshima Astrophysical Science Center, Hiroshima University, Higashi-Hiroshima, Japan. [56]Department of Physics and Astronomy, Louisiana State University, Baton Rouge, LA, USA. [57]Center for Research and Exploration in Space Science and Technology, NASA/GSFC, Greenbelt, MD, USA. [58]Department of Physics, The University of Hong Kong, Hong Kong, China. [59]Department of Astronomy and Astrophysics, Pennsylvania State University, University Park, PA, USA. [60]Université Grenoble Alpes, CNRS, IPAG, Grenoble, France. [61]INAF Osservatorio Astronomico di Brera, Merate, Italy. [62]Dipartimento di Fisica e Astronomia, Università degli Studi di Padova, Padua, Italy. [63]Anton Pannekoek Institute for Astronomy & GRAPPA, University of Amsterdam, Amsterdam, The Netherlands. [64]Guangxi Key Laboratory for Relativistic Astrophysics, School of Physical Science and Technology, Guangxi University, Nanning, China. [65]Unaffiliated: Alexander A. Lutovinov, Sergey V. Molkov, Ilya A. Mereminskiy.
✉e-mail: alexandra.veledina@gmail.com

https://doi.org/10.1038/s41550-024-02294-9

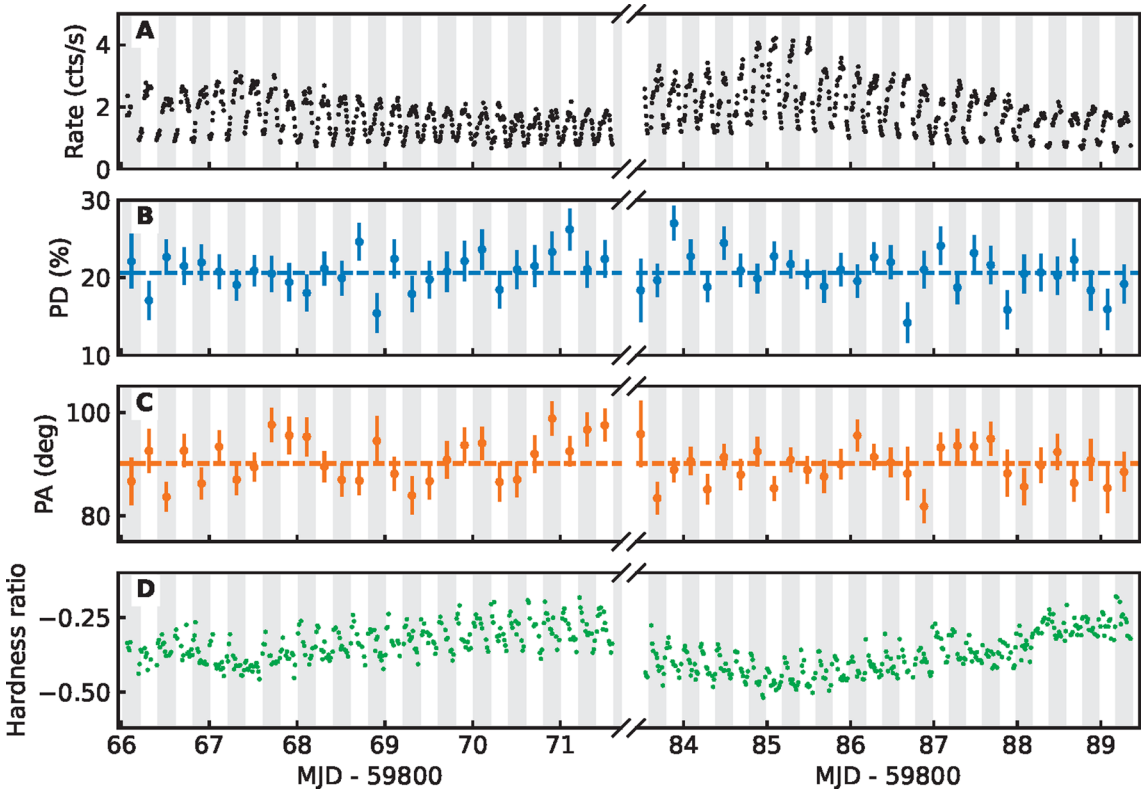

Extended Data Fig. 1 | Variation with time of flux and polarization for the IXPE Main observation. (A) The total rate in the 2–8 keV energy range, binned in time intervals of 500 s. The PD (B) and the PA (C) are averaged over one orbit, as defined by the ephemeris of[21]. Dashed horizontal lines are the average values. (D) The hardness ratio defined as the ratio of the difference in the IXPE count rates in the 4–8 and 2–4 keV energy bands to their sum in 1000 s time bins. Alternating vertical bands identify different orbits. Data are presented as mean values over the time bin and the error bars correspond to 1σ confidence levels.

https://doi.org/10.1038/s41550-024-02294-9

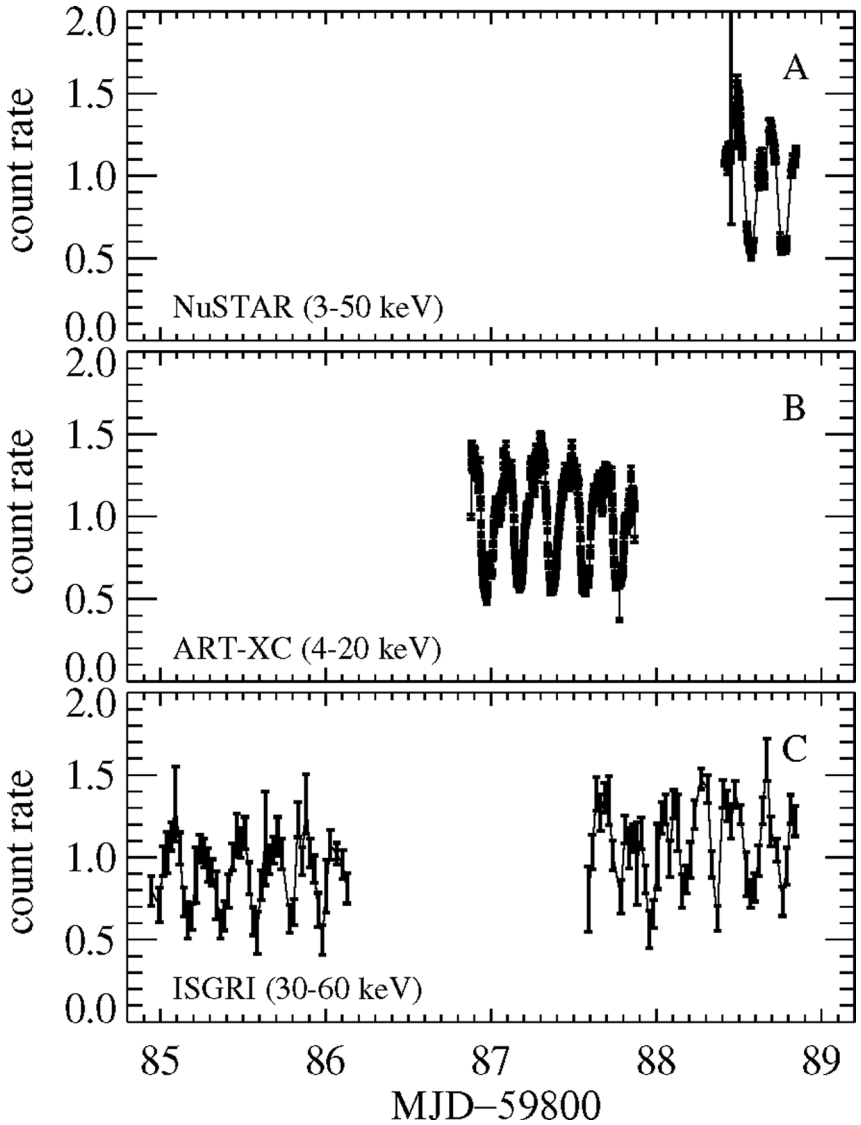

Extended Data Fig. 2 | X-ray light curves of Cyg X-3. X-ray count rates normalised to the average during the Main observation obtained by three X-ray telescopes: NuSTAR (A), SRG/ART-XC (B) and INTEGRAL/ISGRI (C). The IXPE exposure covers the entire duration of the displayed observations.

https://doi.org/10.1038/s41550-024-02294-9

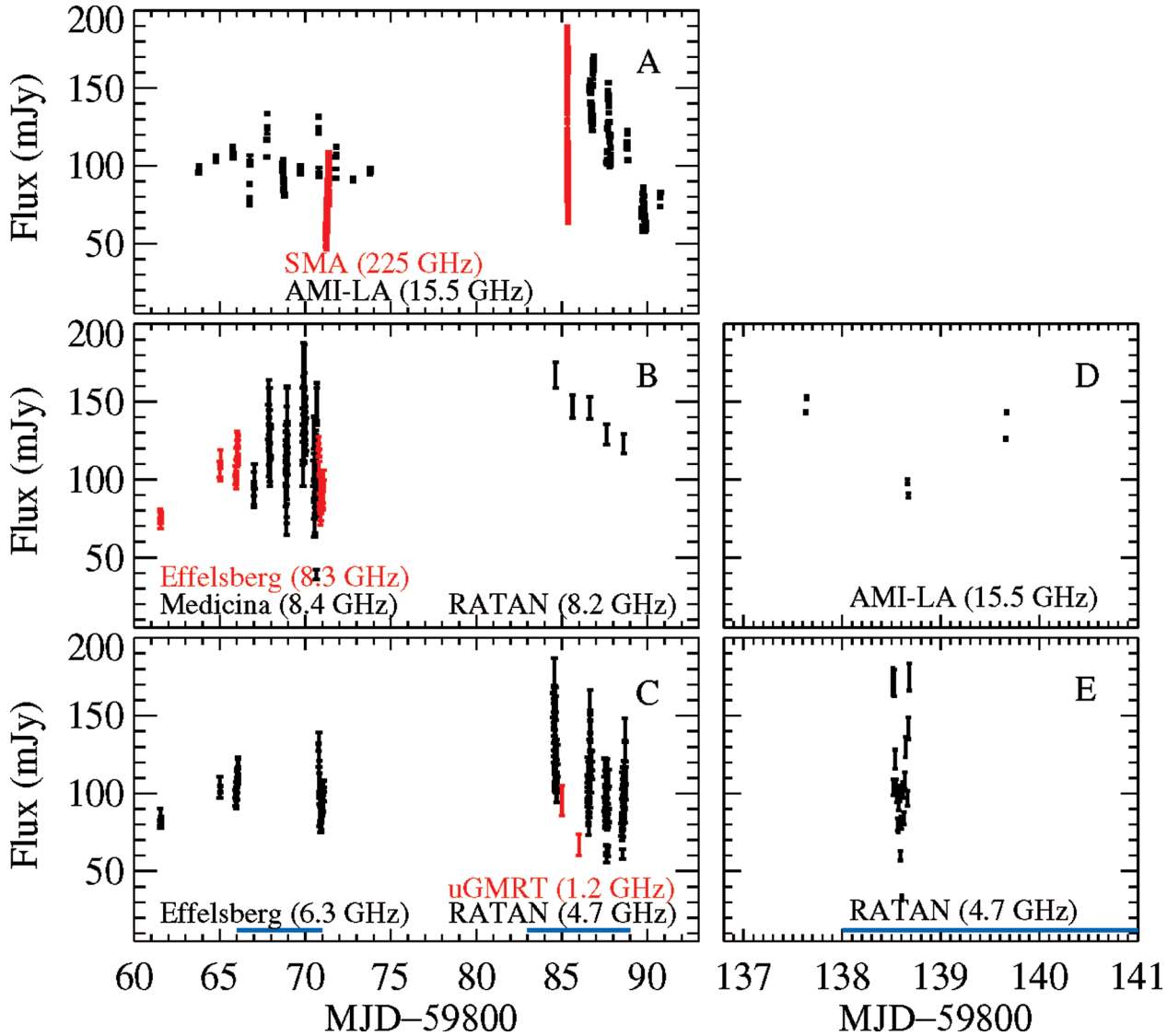

Extended Data Fig. 3 | Radio and sub-mm light curves of Cyg X-3. The light curves of the source around the dates of Main (panels A-C) and ToO (panels D and E) observations, as obtained with various telescopes. IXPE dates are marked with blue stripes. Note high intraday variations of the radio flux caused by the orbital variability. Data are given as the mean values with error bars corresponding to their variance.

https://doi.org/10.1038/s41550-024-02294-9

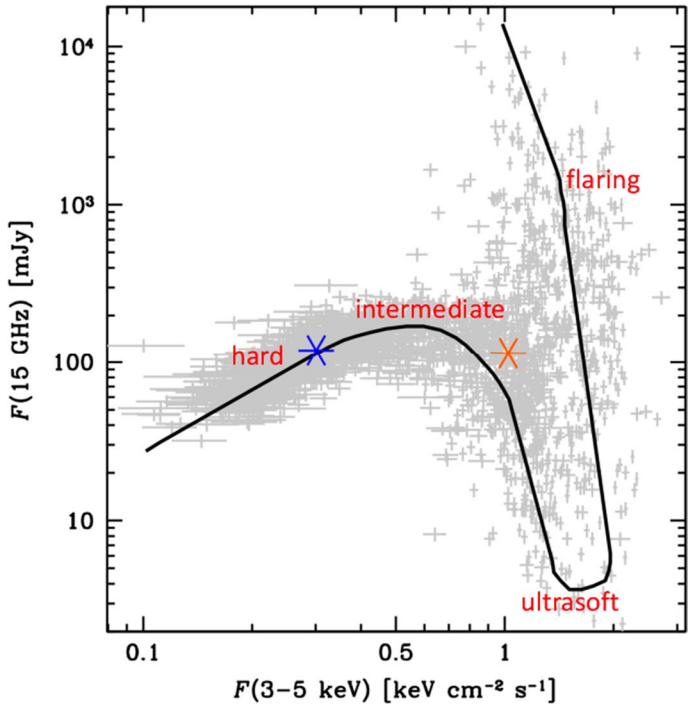

Extended Data Fig. 4 | Radio-X-ray evolution track from historical radio and X-ray observations. Grey points constitute data analysed in[107]. Spectral states are indicated with red. Blue and orange stars indicate the fluxes during the Main and ToO observations, respectively.

https://doi.org/10.1038/s41550-024-02294-9

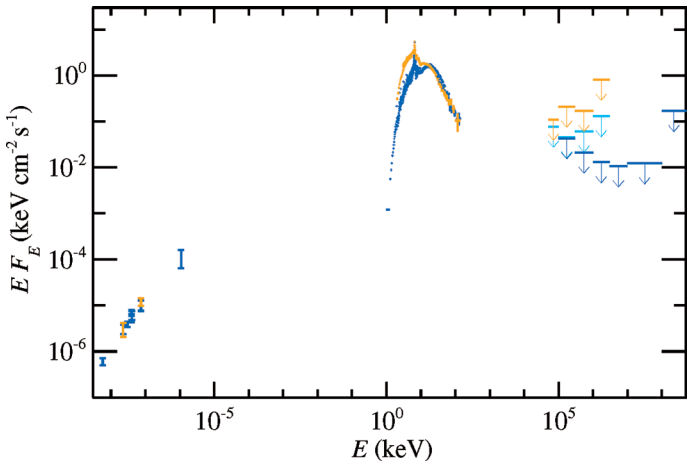

Extended Data Fig. 5 | Broadband spectral energy distribution of Cyg X-3. The SED for the Main (blue) and ToO (orange) observations are from the facilities described in the text. Error bars correspond to 1σ levels.

https://doi.org/10.1038/s41550-024-02294-9

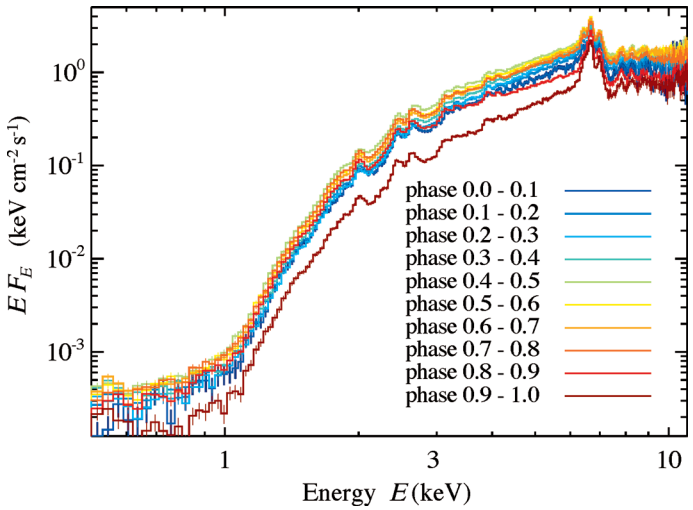

Extended Data Fig. 6 | X-ray SED of Cyg X-3 from NICER. Orbital phase-folded X-ray spectra are taken during the contemporaneous observations in the Main run. Spectra from different phase intervals are presented in different colours.

https://doi.org/10.1038/s41550-024-02294-9

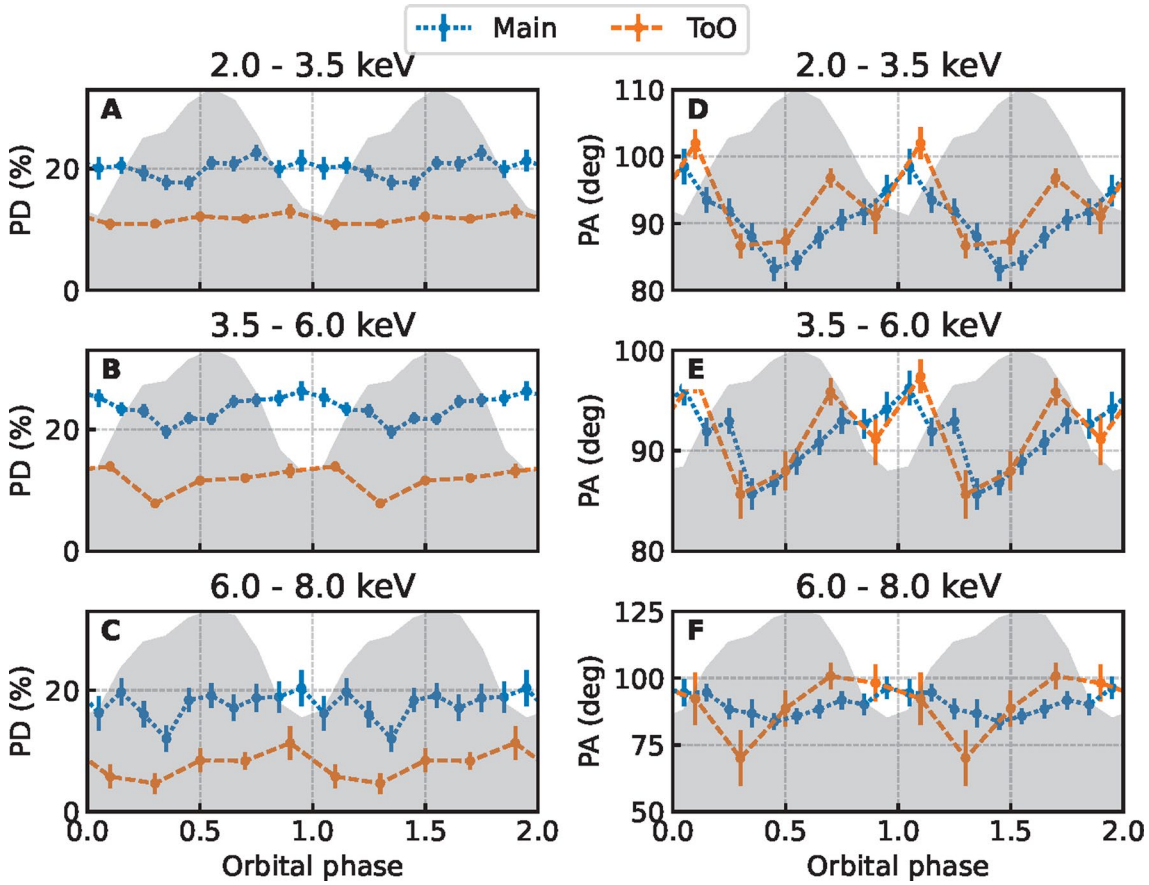

Extended Data Fig. 7 | Orbital phase dependence of polarization. The PD (A)–(C) and PA (D)–(F) in different energy bands (2–3.5 keV, A, D; 3.5–6 keV, B, E; 6–8 keV, C, F) for the Main (in blue) and ToO (in orange) observations are shown. Orbital profiles of IXPE flux are shown in each panel as shaded areas. Error bars correspond to 1σ uncertainty level.

https://doi.org/10.1038/s41550-024-02294-9

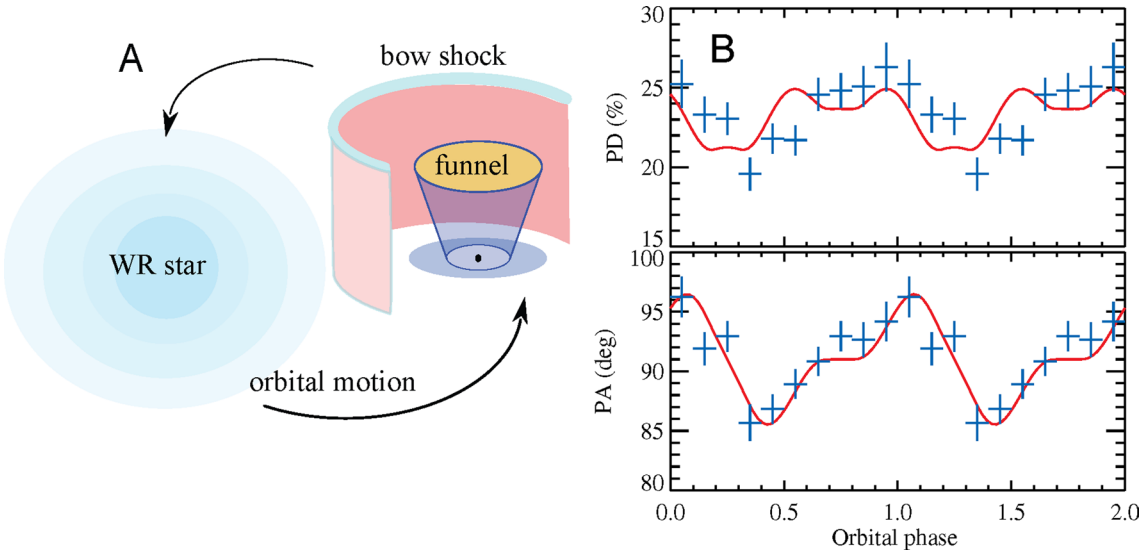

Extended Data Fig. 8 | Modelling orbital variations of the PD and PA. (A) Geometry of the reflector. (B) Dependence of the PD and PA in the 3.5–6 keV band on orbital phase for the Main observation is shown with blue crosses. The red curve is the model of the reflection from a bow shock.

https://doi.org/10.1038/s41550-024-02294-9

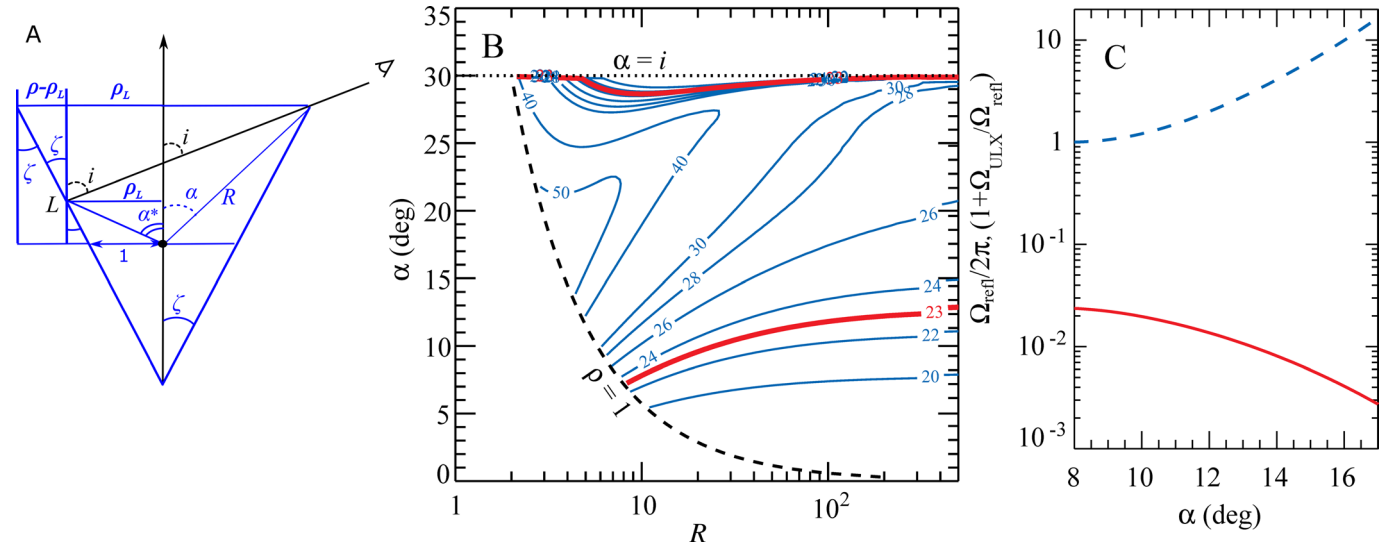

Extended Data Fig. 9 | Detailed geometry of the reflecting funnel, its polarimetric characteristics, reflection and amplification factors. (A) Geometry of the funnel is shown with L being the lowest visible point for the given inclination i, and the angle α^* is its colatitude. (B) The contour plots of constant PD (in %) for the fixed observer inclination ($i = 30^\circ$), as function of the model parameters (α, R). The region above $\alpha = i$ is not allowed because the central source would be visible. The region below $\rho = 1$ curve (that is $R = 1/\sin\alpha$) corresponds to an outflow converging towards the axis, which is not possible. Red contours show the allowed model parameters. (C) Dependence of the solid angle of the reflecting surface ($\Omega_{refl}/2\pi$, red solid curve) and the factor determining the intrinsic luminosity ($1 + \Omega_{ULX}/\Omega_{refl}$, blue dashed curve) on the angle α.

https://doi.org/10.1038/s41550-024-02294-9

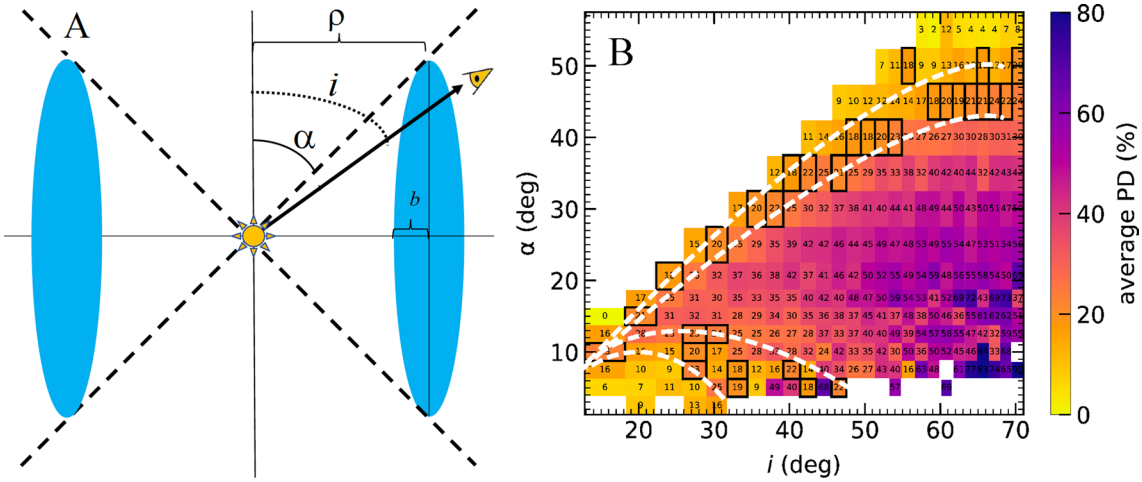

Extended Data Fig. 10 | Results of Monte-Carlo simulations. (A) The geometry of the reflector (elliptical torus in blue) and main parameters of the funnel explored by the Monte-Carlo modelling. (B) The simulated 2–8 keV PD versus observer's inclination and half-opening angle of the torus for $b = \rho/4$, $\tau_e = 7$ and $N_{He} = 8.5 \times 10^{23} cm^{-2}$ (the same display as in Fig. 4 for the analytical model). The black rectangles and white dashed lines mark the regions where the reprocessed component gives PD = 21 ± 3%.